

Multiwavelength investigation of extended green object G19.88-0.53: revealing a protocluster

Namitha Issac,^{1★} Anandmayee Tej,^{1★} Tie Liu,^{2,3} Watson Varricatt,⁴ Sarita Vig,^{5,1} C. H. Ishwara Chandra,⁵ Mathias Schultheis⁶ and Govind Nandakumar^{7,8}

¹Indian Institute of Space Science and Technology, Thiruvananthapuram 695 547, Kerala, India

²Shanghai Astronomical Observatory, Chinese Academy of Sciences, 80 Nandan Road, Shanghai 200030, People's Republic of China

³Key Laboratory for Research in Galaxies and Cosmology, Chinese Academy of Sciences, 80 Nandan Road, Shanghai 200030, People's Republic of China

⁴Institute for Astronomy, UKIRT Observatory, 660 N. Aohoku place, Hilo, HI 96720, USA

⁵National Centre for Radio Astrophysics, Tata Institute of Fundamental Research, Pune University Campus, Pune 411007, India

⁶Laboratoire Lagrange, Université Côte d'Azur, Observatoire de la Côte d'Azur, CNRS, Blvd de l'Observatoire, F-06304 Nice, France

⁷Research School of Astronomy & Astrophysics, Australian National University, ACT 2611, Australia

⁸ARC Centre of Excellence for All Sky Astrophysics in Three Dimensions (ASTRO-3D), Australia

Accepted 2020 July 27. Received 2020 July 27; in original form 2020 April 29

ABSTRACT

A multiwavelength analysis of star formation associated with the extended green object, G19.88-0.53 is presented in this paper. With multiple detected radio and millimetre components, G19.88-0.53 unveils as harbouring a protocluster rather than a single massive young stellar object. We detect an ionized thermal jet using the upgraded Giant Meterwave Radio Telescope, India, which is found to be associated with a massive, dense and hot *ALMA* 2.7 mm core driving a bipolar CO outflow. Near-infrared spectroscopy with UKIRT–UIST shows the presence of multiple shock-excited H₂ lines concurrent with the nature of this region. Detailed investigation of the gas kinematics using *ALMA* data reveals G19.88-0.53 as an active protocluster with high-mass star-forming components spanning a wide evolutionary spectrum from hot cores in accretion phase to cores driving multiple outflows to possible UCH II regions.

Key words: stars: formation – ISM: jets and outflows – ISM: individual objects (G19.88-0.53) – infrared: ISM – infrared: stars.

1 INTRODUCTION

The last decade has seen a plethora of studies focused on understanding the formation mechanism of massive ($M \gtrsim 8M_{\odot}$) stars. Recent reviews by Tan et al. (2014) and Motte, Bontemps & Louvet (2018) detail the significant progress made in the field. State-of-the-art numerical simulations (e.g. Krumholz, Klein & McKee 2007; Kuiper et al. 2010) and tremendous advancement in observational facilities (*Spitzer* Space Telescope, *Herschel* Space Observatory, *ALMA*) have enabled us to probe the intricacies involved and get a better insight of the complex processes associated with high-mass star formation.

Of particular interest are the initial phases of massive star formation, which are observationally the most challenging. The discovery of an interesting population of ‘extended green objects’ (EGOs; Cyganowski et al. 2008; Chambers et al. 2009), with the *Spitzer* Galactic Legacy Infrared Mid-Plane Survey Extraordinaire (Benjamin et al. 2003), has created a unique data base to systematically probe these early phases and aptly constrain the proposed theories. Dedicated studies spanning various frequency regimes have been conducted on EGOs, and they are now regarded as signposts of high-mass star formation where the enhanced, extended emission in the IRAC 4.5 μ m band (colour-coded green in the IRAC colour composite images and hence the nomenclature) is attributed to

shocked emission in outflows from massive young stellar objects (MYSOs).

Several studies have been carried out to decipher the population of identified EGOs (e.g. Marston et al. 2004; Noriega-Crespo et al. 2004; Rathborne et al. 2005; Smith & Rosen 2005), but focused multiwavelength studies towards individual objects are still few. Such studies are crucial in gaining deeper insights into the nature of these objects. In this paper, we conduct a rigorous multiwavelength investigation of the region associated with the EGO, G19.88-0.53, which is catalogued as a ‘likely’ outflow candidate associated with the infrared source, IRAS 18264-1152 (Cyganowski et al. 2008). The kinematic distance ambiguity to G19.88-0.53 has been resolved, and it is placed at the near distance of 3.31 kpc (Roman-Duval et al. 2009; Ge et al. 2014). The bolometric luminosity of the Red MSX Source (RMS), G019.8817-00.5347, associated with IRAS 18264-1152 is estimated to be $7.8 \times 10^3 L_{\odot}$ (Lumsden et al. 2013). This number has been recently refined to $4.7 \times 10^3 L_{\odot}$ in the RMS survey website.¹ Class I and II methanol masers and H₂O maser are detected towards the region (Beuther et al. 2002c; Sridharan et al. 2002; Chen et al. 2011). Fig. 1 displays the infrared (IR) morphology of G19.88-0.53. The colour composite images use the *Spitzer*–IRAC (Fazio et al. 2004) and the UKIDSS–Galactic Plane Survey (Lucas et al. 2008) bands. Both plots show extended emission in the east–west direction with the enhanced IRAC 4.5 μ m emission elongated

* E-mail: namithaissac.16@res.iist.ac.in (NI); tej@iist.ac.in (AT)

¹http://rms.leeds.ac.uk/cgi-bin/public/RMS_DATABASE.cgi

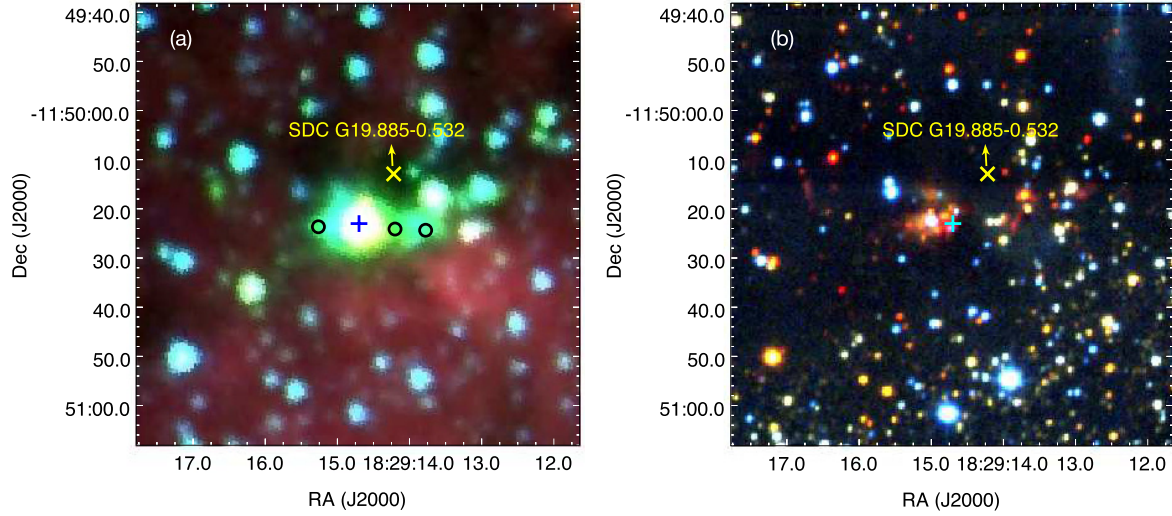


Figure 1. (a) IRAC colour composite image of the region around G19.88-0.53 where the 3.6, 4.5, and 8.0 μm bands are displayed in red, green, and blue, respectively. Location of the identified IRDC is shown with the ‘x’ symbol. The ‘+’ marks the position of the MYSO located at 4.5 μm emission peak and the black circles are the positions of the EGO knots discussed by De Buizer & Vacca (2010). (b) UKIDSS colour composite image of the same region. Here, J (1.25 μm), H (1.63 μm), and K (2.20 μm) band data are shown in red, green, and blue, respectively.

Table 1. GMRT observations and map details for G19.88-0.53.

Details	Band 4	Band 5
Date of Obs.	2018 June 19	2018 June 18
Flux calibrators	3C 286	3C 286
Phase calibrators	1822-096	1743-038
Integration time	~5 h	~5 h
Synthesized beam	~11.5 arcsec \times 7.6 arcsec	~4.3 arcsec \times 2.7 arcsec
rms ($\mu\text{Jy beam}^{-1}$)	100–150	44–47

westwards beyond the UKIDSS K -band nebulosity. The *Simbad* data base also reveals the presence of an infrared dark cloud (IRDC) possibly associated with G19.88-0.53 and is marked in the figure.

The structure of the paper, which involves an in-depth observational study of the region associated with G19.88-0.53 at infrared, submillimeter, and radio wavelengths, is as follows. New observations carried out by us, and the archival data used are discussed in Section 2; the data reduction procedures are also included in this section. Results obtained from multiwavelength data are highlighted in Section 3. In Section 4, we deliberate on the observational evidence of the presence of a protocluster and the existence of an ionized jet, and discuss on the kinematics of the identified dust cores. Section 5 summarizes the results and discussion.

2 OBSERVATIONS AND ARCHIVAL DATA

2.1 Radio continuum observation

Low-frequency radio emission associated with G19.88-0.53 is studied with the upgraded Giant Meterwave Radio Telescope (uGMRT), located near Pune, India. Observations for G19.88-0.53 were carried out in Band 4 (550–850 MHz) and Band 5 (1000–1450 MHz). Observation and map details are listed in Table 1. The data were calibrated incorporating spectral index and spectral curvature across the wide band using the Astronomical Image Processing System (AIPS). Data reduction is carried out along the lines discussed in

Issac et al. (2019). We refer the reader to this paper for an elaborate discussion of GMRT configuration and data reduction steps. In case of G19.88-0.53, calibrated and channel averaged data are split into sub-bands of bandwidth ~ 32 and ~ 36 MHz in Bands 4 and 5, respectively. This is done with the envisaged goal of obtaining in-band spectral index of the radio source. We retain six clean sub-bands in Band 4 and three in Band 5, with central frequencies 651.4, 682.5, 714.1, 745.9, 777.1, and 808.3 MHz and 1320.7, 1355.8, and 1391.6 MHz, respectively. Continuum maps for each sub-band were generated separately by limiting the uv coverage to a common range of 0.15–36 K λ with beams matched to 11.5 arcsec \times 7.6 arcsec, the largest beam among the six sub-bands. Similarly, for Band 5 the uv range is fixed to 0.17–100 K λ and beams matched to 4.3 arcsec \times 2.5 arcsec. As discussed in Issac et al. (2019), scaling factors are estimated to range between 1.65 to 2.10 and 1.22 to 1.24 within Bands 4 and 5, respectively. Using these, the primary beam corrected and self-calibrated sub-band maps are scaled to account for variations in the system temperatures of the antennas at the GMRT while observing targets located in the Galactic plane.

2.2 Near-infrared spectroscopic observation

We carried out the near-infrared (NIR) spectroscopic observations towards G19.88-0.53 with the 3.8-m United Kingdom Infrared Telescope (UKIRT), Hawaii. Observations were obtained on 2015 April 2 with the UKIRT 1–5 μm Imager Spectrometer (UIST; Ramsay Howat et al. 2004) using the HK grism set-up. The slit (~ 0.48 arcsec wide and 120 arcsec long) was oriented at an angle 88° east of north and centered at ($\alpha_{J2000} = 18^{\text{h}}29^{\text{m}}14^{\text{s}}.7$, $\delta_{J2000} = -11^\circ50'16''.7$) as shown in Fig. 3. The exposure time per frame was 120 s and the total on-source integration time was 720 s. SAO 142372, an A5 IV/V type star, was also observed, with the same instrument settings as for the target, for telluric and instrumental corrections. Following the standard procedures explained in Issac et al. (2019), UKIRT pipeline ORAC-DR and Starlink packages FIGARO and KAPPA were used for data reduction, spectra extraction, and wavelength calibration. As

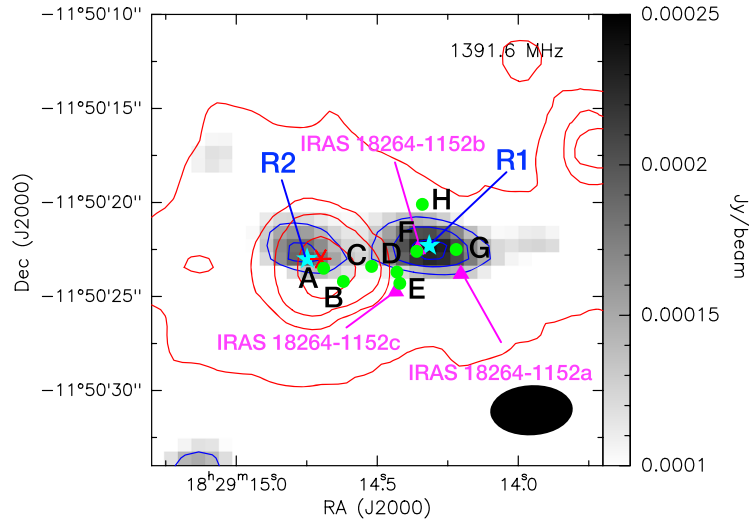


Figure 2. The radio continuum map of G19.88-0.53 at 1391.6 MHz is shown in grey scale with contour levels at 3, 4, 5, and 6σ ($\sigma = 45 \mu\text{Jy beam}^{-1}$). This map has a beam size of $4.3 \text{ arcsec} \times 2.7 \text{ arcsec}$ that is represented by the black ellipse. The positions of the two radio components, R1 and R2 are marked on the image by ‘*’s. Radio sources A–H, identified by Rosero et al. (2016), are marked by the filled circles and the three radio components IRAS 18264-1152a, IRAS 18264-1152b, and IRAS 18264-1152c, identified by Zapata et al. (2006), are indicated by the filled triangles. Contours of the $4.5 \mu\text{m}$ emission are overlaid in red with the contour levels at 3, 9, 30, and 120σ ($\sigma = 5.0 \text{ MJy sr}^{-1}$). The position of the MYSO (De Buizer & Vacca 2010) associated with G19.88-0.53 is indicated with ‘*’.

the sky conditions during our observations were not photometric, the final spectra are not flux calibrated.

2.3 Far-infrared data from Hi-GAL survey

To understand the physical properties of the cold dust emission associated with G19.88-0.53, we use *Herschel* far-infrared (FIR) archival data. The *Herschel Space Observatory* houses a 3.5-m telescope with instruments covering the spectral range of 55–671 μm (Pilbratt et al. 2010). For our study, we have utilized observations carried out with the Photodetector Array Camera and Spectrometer (Poglitsch et al. 2010) and Spectral and Photometric Imaging Receiver (Griffin et al. 2010). The 70–500 μm images retrieved were observed as a part of the *Herschel* infrared Galactic plane Survey (Hi-GAL, Molinari et al. 2010). The images have resolutions of 5, 13, 18.1, 24.9, and 36.4 arcsec at 70, 160, 250, 300, and 500 μm , respectively.

2.4 APEX + Planck data

APEX + *Planck* data base provides 870 μm images. These are generated by combining 870 μm LABOCA bolometer array data from the APEX Telescope Large Area Survey of the Galaxy (ATLASGAL; Schuller et al. 2009) and 850 μm data from *Planck*/HFI. The combined data set offers improved spatial dynamic range of Galactic cold dust emission (Csengeri et al. 2016). The retrieved APEX + *Planck* image of the region associated with G19.88-0.53 has pixel size of 3.4 arcsec and angular resolution of 21 arcsec.

2.5 Atacama Large Millimeter Array archival data

Atacama Large Millimeter Array (ALMA) archival data at 2.7 mm (Band 3) and 870 μm (Band 7) are used to study the G19.88-0.53 complex. Observations were made during 2017-2018 (PI: S. Leurini #2017.1.00377.S). The high- and medium-resolution ALMA observations were obtained with the 12-m array in the FDM Spectral Mode and the low-resolution observations used the 7-m array in

the ACA Spectral Mode. The high-resolution 2.7 mm continuum map, with a beam size of $0.46 \text{ arcsec} \times 0.28 \text{ arcsec}$, is used to identify the compact dust cores associated with G19.88-0.53. Along with the continuum observations, data cubes in both the bands are also retrieved. Three data sets with resolutions $16.9 \text{ arcsec} \times 8.0 \text{ arcsec}$, $2.6 \text{ arcsec} \times 2.2 \text{ arcsec}$, and $0.46 \text{ arcsec} \times 0.28 \text{ arcsec}$ and velocity resolution of 0.67 km s^{-1} in Band 3 (84–116 GHz) and two data sets with resolutions $5.2 \text{ arcsec} \times 2.6 \text{ arcsec}$ and $0.67 \text{ arcsec} \times 0.47 \text{ arcsec}$ and velocity resolution of 0.86 km s^{-1} in Band 7 (275–373 GHz) are used. In Band 3, *rms* of 4.2, 3.6, and 17 mJy are achieved for high-, medium-, and low-resolution observations, respectively. In Band 7, *rms* of 3.5 and 17 mJy are achieved for high- and low-resolution observations, respectively. Analysis of molecular line data is carried out using CLASS90 (Continuum Line Analysis Single-dish Software), a GILDAS² software (Grenoble Image and Line Data Analysis Software).

3 RESULTS

3.1 Low-frequency radio emission

Using the uGMRT, we probe the low-frequency domain of the ionized emission associated with G19.88-0.53. In Band 4, none of the sub-band images have detection above the 3σ level while faint, elongated emission is seen in the Band 5 maps. The deep uGMRT maps in Band 5 with an *rms* level of $\sim 45 \mu\text{Jy beam}^{-1}$ enable the detection of weak ionized emission. In comparison, there is no emission detected in the Very Large Array (VLA) 20 cm map from MAGPIS. The sub-band image at 1391.6 MHz is shown in Fig. 2. This map clearly reveals the presence of an elongated, two-component emission feature in the east–west direction. The two distinct and compact radio components are labelled R1 and R2. The contours of the $4.5 \mu\text{m}$ emission plotted show that the radio emission is confined to the central part of the EGO.

²<http://www.iram.fr/IRAMFR/GILDAS>

Table 2. Physical parameters of radio components R1 and R2 associated with G19.88-0.53.

Component	Peak position		Peak flux density (mJy beam ⁻¹)
	α (J2000) (h m s)	δ (J2000) (° ′ ″)	
R1	18 29 14.3	-11 50 22.3	0.25 ± 0.01
R2	18 29 14.7	-11 50 23.0	0.20 ± 0.01

The radio emission associated with G19.88-0.53 has been studied by Zapata et al. (2006) and Rosero et al. (2016, 2019) using VLA. Based on observations at 3.6 cm (8.5 GHz), 1.3 cm (22.5 GHz), and 7 mm (43.3 GHz), Zapata et al. (2006) classify this source as a ‘triple stellar system’ and identify three radio components (IRAS 18264-1152a, b, and c), the positions of which are shown in Fig. 2. In the recent paper, Rosero et al. (2016) present high-sensitivity, sub-arcsecond resolution observations at 6 cm (4.9 and 7.4 GHz) and 1.3 cm (20.9 and 25.5 GHz), where 12 compact radio sources are detected towards G19.88-0.53. Eight among them, sources A–H, lie within the 3σ level of the $4.5\ \mu\text{m}$ emission and are marked Fig. 2. The component R1 is co-spatial (within ~ 1 arcsec) with the radio sources, F and IRAS 18264-1152b. Component R2 has similar positional match with the radio source, A. The position of the MYSO located at the $4.5\ \mu\text{m}$ emission peak (De Buizer & Vacca 2010) also agrees well with the coordinates of R2. However, this component is not detected in the VLA maps presented by Zapata et al. (2006).

The position of the components and the peak flux densities are listed in Table 2. Component R1 is barely resolved and component R2 is unresolved in the uGMRT maps. It is thus difficult to get a reliable estimate of the integrated flux density for these unresolved sources with weak emission (Urquhart et al. 2009; Rosero et al. 2016). Hence, in the estimation of the spectral index we use the peak flux density. Following the discussion in Urquhart et al. (2009), the upper limits to the deconvolved sizes of R1 and R2 are taken to be half the full width at half-maximum (FWHM) of the restored beam size. This gives a value of $2.1\ \text{arcsec} \times 1.3\ \text{arcsec}$ for the components.

3.2 Near-infrared line emission

As propounded by several authors (and references therein Caratti o Garatti et al. 2015), shock-excited lines of H_2 and [FeII] and broad bandheads of CO are the spectral carriers responsible for the enhanced $4.5\ \mu\text{m}$ emission of EGOs. Of the few spectroscopic studies of EGOs (e.g. De Buizer & Vacca 2010; Caratti o Garatti et al. 2015; Onaka et al. 2016; Issac et al. 2019), De Buizer & Vacca (2010) focused on mid-infrared (MIR) spectroscopy of two EGOs including G19.88-0.53 using the Near-Infrared Imager instrument on the Gemini North telescope. The spectra extracted towards the three associated knots of G19.88-0.53 show the presence of the shock-excited 0–0 S(9) line of H_2 at $4.695\ \mu\text{m}$. Moreover, no continuum emission was detected towards these knots. In our study, we investigate the NIR regime to identify shock indicators and confirm the association of G19.88-0.53 with protostellar outflows.

The H_2 line image towards G19.88-0.53, presented in Varricatt et al. (2010) reveals the presence of a bipolar outflow in the east–west direction, which is consistent with CO outflow detected by Beuther et al. (2002b). Same results were obtained by Lee et al. (2012) using the UWISH2 survey and they enlist G19.88-0.53 as an EGO with a large-scale (angular scale of ~ 1.6 arcmin) bipolar outflow. In Fig. 3, we display the continuum-subtracted H_2 line image from Varricatt et al. (2010) where the orientation of the slit position for UIST observations is marked. The identified apertures, K1, K2, and

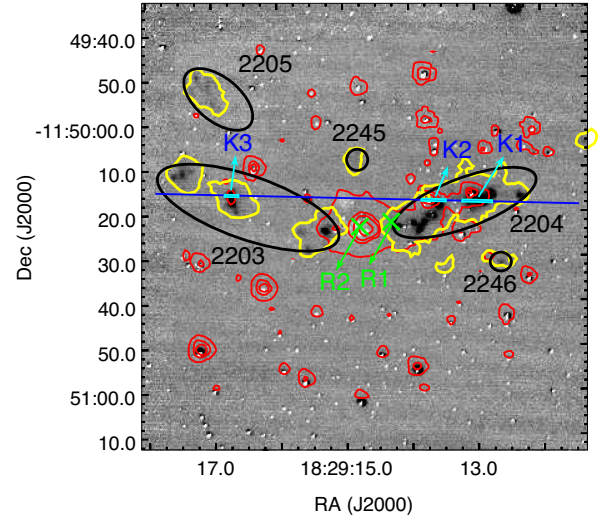


Figure 3. Continuum subtracted H_2 image of G19.88-0.53 from Varricatt et al. (2010). The positions of the identified radio components, R1 and R2 are marked by ‘x’s. The contours of the $4.5\ \mu\text{m}$ emission are given in red with the contour levels same as Fig. 2. The blue line indicates the orientation of the slit and the cyan rectangles are the apertures over which the spectra are extracted. The MHOs (2203-2205, 2245, 2246) identified by Varricatt et al. (2010), Lee et al. (2012), and Ioannidis & Froebrich (2012) are highlighted in the black ellipses. The yellow contours trace the location and extent of the H_2 knots identified by Froebrich et al. (2011).

Table 3. Lines detected in the spectra extracted along the apertures K1, K2, and K3 towards G19.88-0.53.

Line	Wavelength (μm)
$\text{H}_2\ 1-0\ \text{S}(7)$	1.7480
$\text{H}_2\ 1-0\ \text{S}(6)$	1.7880
$\text{H}_2\ 1-0\ \text{S}(5)$	1.8358
$\text{H}_2\ 1-0\ \text{S}(4)$	1.8920
$\text{H}_2\ 1-0\ \text{S}(3)$	1.9576
$\text{H}_2\ 1-0\ \text{S}(2)$	2.0338
$\text{H}_2\ 2-1\ \text{S}(3)$	2.0735
$\text{H}_2\ 1-0\ \text{S}(1)$	2.1218
$\text{H}_2\ 1-0\ \text{S}(0)$	2.2235
$\text{H}_2\ 2-1\ \text{S}(1)$	2.2477

K3, over which the spectra are extracted are also highlighted in the figure. Molecular hydrogen objects (MHOs) from the catalogue of molecular hydrogen emission-line objects³ (Davis et al. 2010) are also indicated. MHO 2245 and MHO 2246 are new additions to the catalogue by Lee et al. (2012) and Ioannidis & Froebrich (2012), respectively. Identified locations and extent of H_2 knots from Froebrich et al. (2011) are also shown in the figure. Apertures K1 and K2 probe the knots in MHO 2204 and K3 samples the central knot in MHO 2203. The extracted spectra are shown in Fig. 4 where we see strong detections of several H_2 lines. The lines detected and their corresponding wavelengths are listed in Table 3.

The H_2 lines detected in the spectra could have either a thermal or a non-thermal origin. Jets and outflows that are heated to typically few 1000 K can give rise to thermal emission from shock fronts, whereas non-thermal emission is ascribed to fluorescence produced

³<http://cdsweb.u-strasbg.fr/cgi-bin/qcat?J/A+A/511/A24>

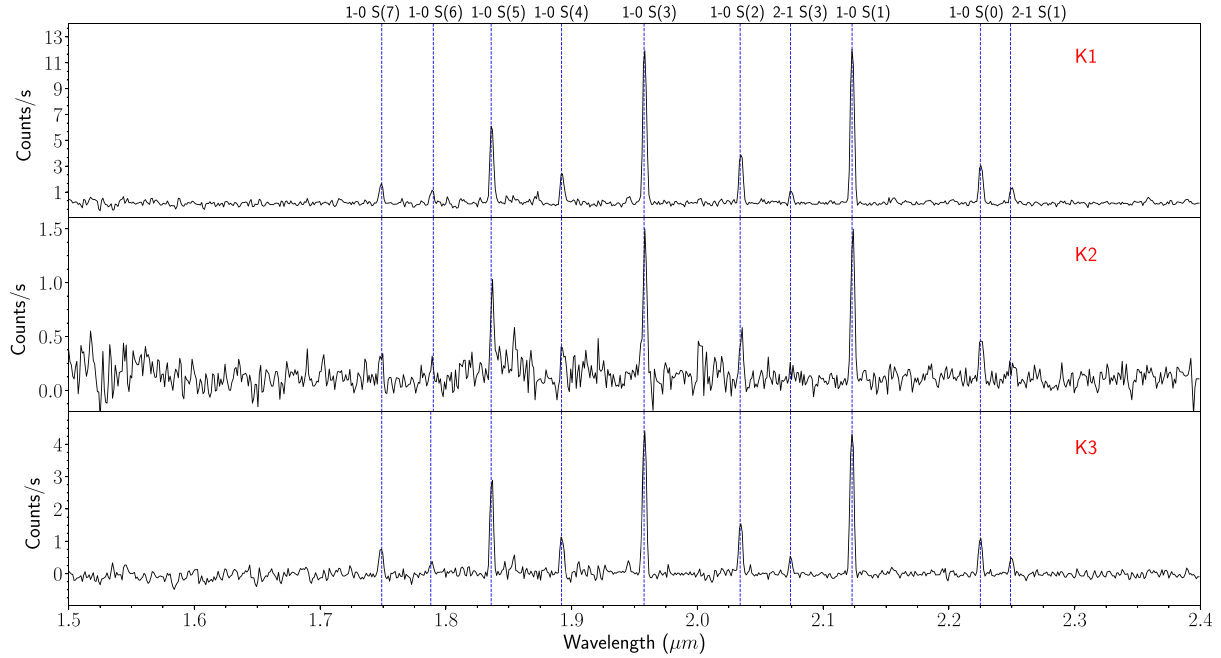


Figure 4. The *HK* spectrum of G19.88-0.53 extracted over the apertures K1, K2, and K3 covering three H_2 knots (refer Fig. 3). The spectral lines identified along all the three apertures are marked over the spectra and the details of these lines are given in Table 3.

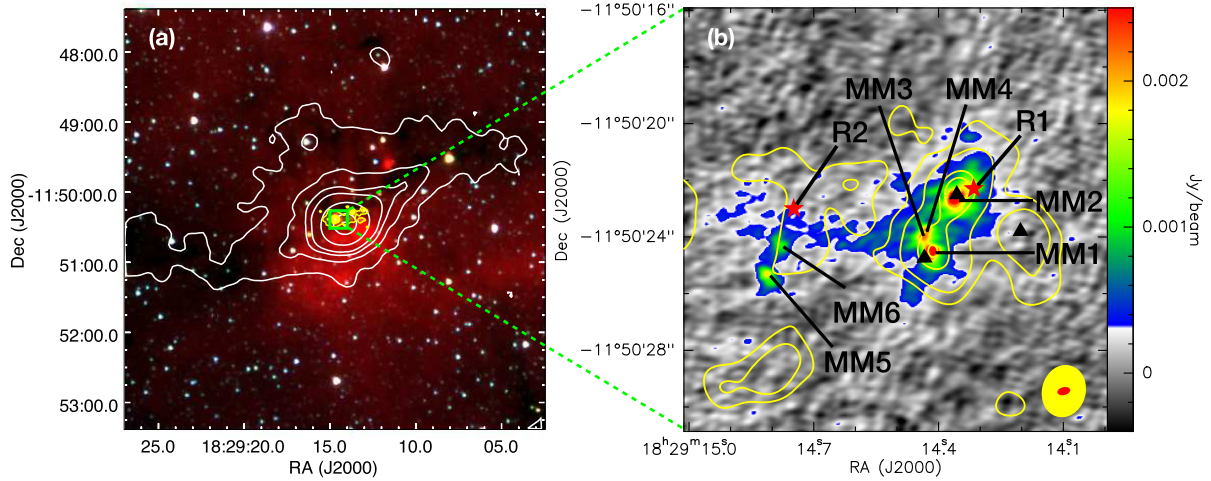


Figure 5. (a) Colour composite image of the region associated with G19.88-0.53, using IRAC 3.6 μm (blue), 4.5 μm (green), and 8.0 μm (red) bands. The white contours depict the APEX + Planck 870 μm emission with levels 2, 3, 4, 5, 9, 20, and 26σ ($\sigma = 0.3 \text{ Jy beam}^{-1}$). The yellow contours represent the 4.5 μm emission with the contour levels same as in Fig. 2. (b) The high resolution 2.7 mm *ALMA* map towards G19.88-0.53 is depicted in the colour scale. The positions of the two radio components and the 6 mm peaks identified are marked on the map. The yellow contours represent emission at 7 mm from Zapata et al. (2006) with contour levels at 4, 8, 18, 22, and 26σ ($\sigma = 53.8 \mu\text{Jy beam}^{-1}$). The filled black triangles are the positions of the radio peaks identified by these authors. The beams of the 2.7 and 7 mm maps are shown as filled red and yellow ellipses, respectively, towards the bottom right of the image.

Table 4. Physical parameters derived for the clump identified to be associated with G19.88-0.53. The peak position of the 870 μm emission, radius, mean temperature and column density, mass, and volume number density of the clump are listed.

Peak position $\alpha(\text{J2000}) (^{\text{h}} \text{ m s})$	Peak position $\delta(\text{J2000}) (^{\circ} ' ")$	Radius (pc)	Mean T_d (K)	Mean $N(\text{H}_2)$ (10^{22} cm^{-2})	Mass (M_{\odot})	Number density, $n(\text{H}_2)$ (10^3 cm^{-3})
18 29 14.14	-11 50 28.57	0.7	18.6 ± 1.2	5.3 ± 1.0	1911	18.0

Table 5. Physical parameters of the 2.7 mm cores associated with G19.88-0.53.

Core	Peak position		Deconvolved size (arcsec \times arcsec)	Integrated flux density (mJy)	Peak flux density (mJy/beam)	V_{LSR} (km s $^{-1}$)	ΔV (km s $^{-1}$)
	RA (J2000) ($^{\text{h}} \text{ } ^{\text{m}} \text{ } ^{\text{s}}$)	Dec. (J2000) ($^{\circ} \text{ } ' \text{ } ''$)					
MM1	18 29 14.4	−11 50 24.5	0.65×0.44	10.7	3.4	44.2	6.0
MM2	18 29 14.4	−11 50 22.6	1.49×0.94	30.9	3.5	45.3	5.7
MM3	18 29 14.4	−11 50 24.0	0.98×0.50	11.9 ^a	2.3 ^a	43.3 ^a	4.5 ^a
MM4	18 29 14.4	−11 50 23.7	0.98×0.50	11.9 ^a	2.3 ^a	43.3 ^a	4.5 ^a
MM5	18 29 14.8	−11 50 25.3	0.74×0.26	5.4	1.9	43.3	2.3
MM6	18 29 14.8	−11 50 24.3	0.62×0.46	3.9	1.1	42.3	1.6

^aMM3 and MM4 are unresolved in the map, hence the quoted deconvolved size, integrated, peak flux density, LSR velocity, and velocity width refer to the combined region covering both the cores.

by non-ionizing UV photons. Shock excited emission arises from low levels of excitation, whereas UV fluorescence populates both high- and low- v states (Davis et al. 2003; Caratti o Garatti et al. 2015). Our spectra do not show the presence of transitions with $v \geq 6$. In addition, the ratio of $1 - 0 \text{ S}(1)/2 - 1 \text{ S}(1)$ is estimated to be $\sim 8:1$. These suggest the origin of the detected H_2 lines to be due to thermal excitation. However, the absence of relevant fluorescent H_2 emission in G19.88-0.53 can also be attributed to high extinction that screens the UV photons emanating from the central star. None the less, morphological resemblance of the extended H_2 emission knots to a bipolar jet and the association with an outflow source supports the shock excitation scenario. The shock-excited origin of the detected H_2 lines confirms that the transitions of this molecule within the IRAC 4.5 μm band are among the spectral carriers responsible for the enhanced ‘green’ emission that classifies G19.88-0.53 as an EGO.

3.3 Emission from dust

IRAC bands trace the thermal emission associated with the warm dust component and emission from the polycyclic aromatic hydrocarbons excited by the UV photons in the photodissociation regions. However, emission from the stellar photosphere dominates the shorter wavelength bands (3.6 and 4.5 μm ; Watson et al. 2008). In addition to this, the 4.5 μm band includes emission from shock-excited H_2 lines and CO ($v = 1 - 0$) band at 4.6 μm with contribution from the Br α and Pf β lines. The spatial distribution of dust emission towards G19.88-0.53 is shown in Fig. 5(a), which is a colour composite image generated using the IRAC 8.0, 4.5, and 3.6 μm bands. The APEX + Planck 870 μm contours are overlaid along with the contours of the 4.5 μm emission. A clump is clearly identified at 870 μm . Warm dust sampled at 8.0 μm is seen to be extended towards the south and west of the clump and, at 870 μm , a clearly discernible large-scale filamentary structure is visible with the clump located within it.

3.3.1 Dust clump

From the APEX + Planck 870 μm map, a clump is identified using the 2D *Clumpfind* procedure (Williams, de Geus & Blitz 1994) with a 3σ ($\sigma = 0.3 \text{ Jy beam}^{-1}$) threshold and optimum contour levels. The aperture of this clump coincides with the 3σ level contour of the 870 μm emission. To investigate the nature of the cold dust associated with the identified clump, we assume the FIR emission to be optically thin and model the same with a modified single-temperature blackbody following the formalism discussed in detail in Issac et al. (2019). The SED and the best-fitting modified blackbody are shown in Fig. 6. The model derived dust temperature and line-of-sight column density values are $18.6 \pm 1.2 \text{ K}$ and $5.3 \pm 1.0 \times 10^{22} \text{ cm}^{-2}$,

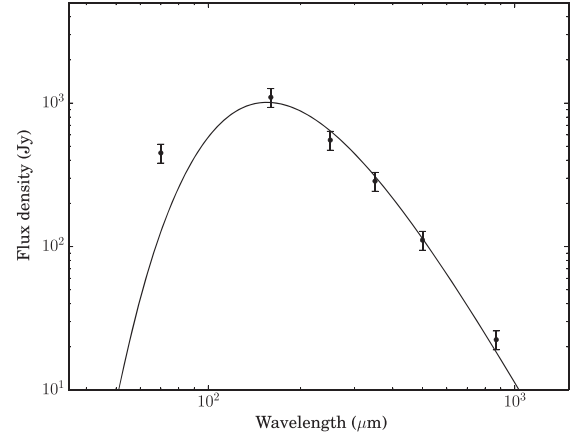


Figure 6. Spectral energy distribution of the APEX + Planck clump associated with G19.88-0.53 in the wavelength range 70–870 μm . The integrated flux density within the clump, represented by the black circles is plotted in log-scale with a 15 percent error bar. The best-fitting modified blackbody model is represented by the solid curve. The data point corresponding to 70 μm is excluded in the SED fitting.

respectively. The mass of the clump is estimated to be $1911 M_{\odot}$. This is in good agreement with the estimate of $\sim 2100 M_{\odot}$ derived by Beuther et al. (2002a, 2005) from the 1.2 mm emission. Both these values derived from dust emission are lower by a factor of ~ 2 in comparison with the value of $3900 M_{\odot}$ obtained from the H^{13}CO^+ line emission (Qiu et al. 2007). The discrepancy could be due to the fact that the H^{13}CO^+ line traces the lower density gas and could even be slightly optically thick as opposed to the optically thin assumption we have employed while estimating the clump mass. Moreover, the H^{13}CO^+ is likely to be affected by outflows and shocks associated with the clump. The derived clump parameters are listed in Table 4.

3.3.2 Millimeter cores

The high-resolution ALMA 2.7 mm dust continuum map displayed in Fig. 5(b) shows the presence of six dense, compact dust cores labelled MM1 – MM6. Contours of the 7 mm VLA map from the study by Zapata et al. (2006) is overlaid on the image. The 7 mm emission is more extended, especially in the east–west direction. In an earlier study, Qiu et al. (2007) have mapped IRAS 18264-1152 at 1.3 and 3.4 mm with Plateau de Bure Interferometer. They identify two peaks at both the wavelengths. Their western peak seems to be in the vicinity of cores, MM1 – MM4 and the eastern component is likely to be associated with cores, MM5 and MM6. Parameters of the identified mm cores are listed in Table 5. The deconvolved sizes of the cores are estimated by fitting 2D Gaussians to each component using

the 2D fitting tool of CASA viewer. MM3 and MM4 are unresolved in the map, hence the quoted size, integrated, and peak flux density refer to the combined region covering both the cores.

3.4 Molecular line emission

Molecular line observations are tools for understanding the kinematics and chemical environment of a molecular cloud and its stage in the evolutionary sequence. In this work, we use archival data from *ALMA* to study the emission from molecular lines in the region associated with G19.88-0.53.

3.4.1 CH₃OH line emission

A forest of CH₃OH lines is detected towards the mm cores in *ALMA* Band 7 (275–373 GHz) within a frequency interval of 3 GHz (337.1–340.1 GHz). This is expected as the CH₃OH molecule is believed to be present in massive star-forming regions from the very early stages (Wirström et al. 2011). For identification of the lines, the data cube is corrected for the LSR velocity of 43.6 km s^{−1} (Beuther et al. 2002a; Qiu et al. 2007). Subsequently, the detected lines are identified by comparing with the rest frequencies reported in the molecular data bases, NIST⁴ (Lavas 2004), CDMS⁵ (Müller et al. 2005), and JPL⁶ (Pickett et al. 1998). The CDMS and JPL data bases are interactively loaded on the spectra employing the Weeds extension of CLASS90. The extracted spectra towards the mm cores are plotted in Fig. 7 displaying the identified set of *A* – and *E* – CH₃OH lines corresponding to the *J* = 7 – 6 transition. It should be noted here that for cores MM3 and MM4, the separation is less than the beam size, hence the combined spectrum is plotted in the figure. CH₃OH lines are seen to be much stronger towards MM1 and MM2 as compared to the other cores. The accurate identification of the detected lines enables us to determine the LSR velocities of the individual cores, which are listed in Table 5.

3.4.2 Emission in isotopologues of CO

In the *ALMA* Band 3 (84 – 116 GHz) and Band 7 (275 – 373 GHz), we detect three CO transitions, ¹³CO(1 – 0), C¹⁸O(1 – 0), and C¹⁷O(3 – 2), with rest frequencies 110.2013543, 109.7821734, and 337.7061123 GHz, respectively. The rotational transition lines of the isotopologues of CO are well-known tracers of both outflow and inflow motion (Kutner & Tucker 1975; Zhang et al. 2001; Beuther et al. 2002b; Wu et al. 2009). Transitions from different energy levels probe the kinematic structure of different parts of the molecular clouds. Since transitions from higher rotational levels of CO molecules have a higher critical density, their emission arises from high-density regions such as the dense cores. On the other hand, emission lines corresponding to lower *J* transitions trace the kinematics of the low-density regions of the molecular cloud (Rygl et al. 2013).

Low-resolution spectra probing the ¹³CO(1 – 0) and C¹⁸O(1 – 0) molecular line emission are plotted in Fig. 8. The beam covers all the cores. Single Gaussians are used to fit these spectra. The ¹³CO(1 – 0) line peaks at the LSR velocity of the dust clump. Multiple peaks noticeable in C¹⁸O(1 – 0) spectrum are the combined effect of the cores and the peak velocities are consistent with the LSR velocities

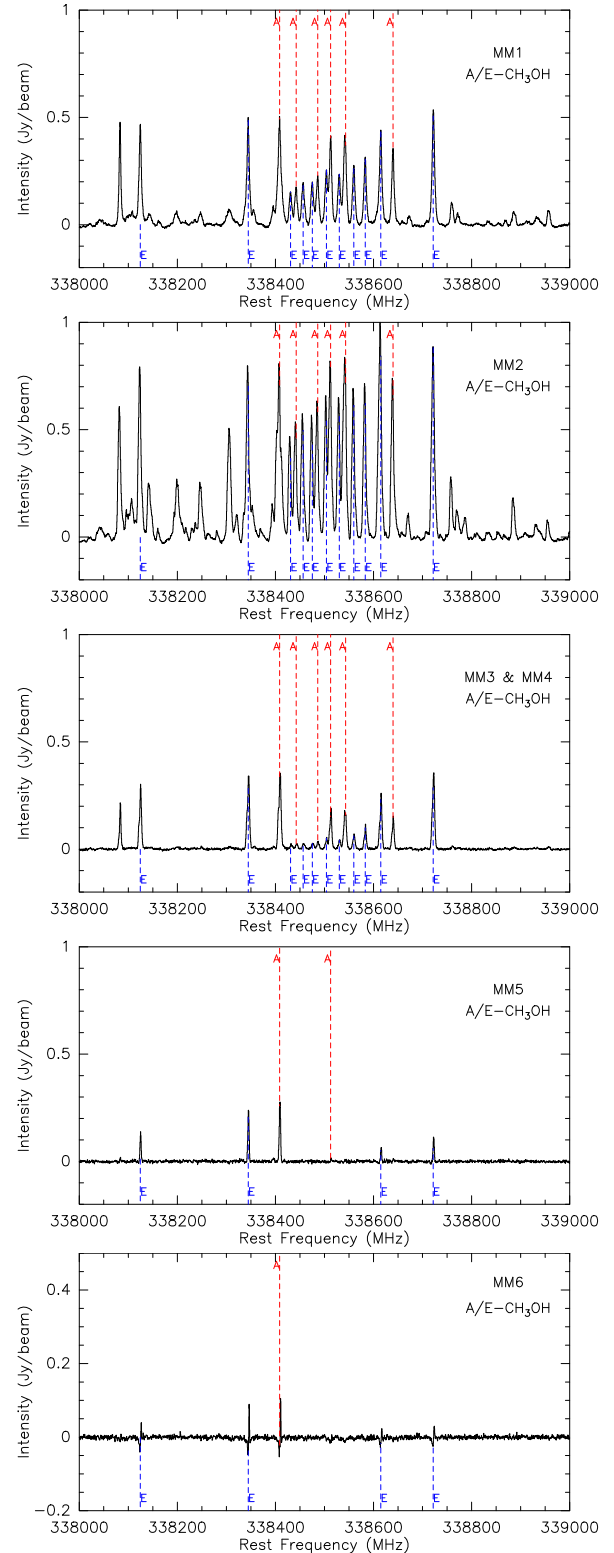


Figure 7. Spectra of the *A/E* – CH₃OH lines detected towards the mm cores associated with G19.88-0.53 extracted from the high-resolution Band 7 spectral cube. The dashed red and blue lines indicate the peak positions of the *A* – CH₃OH and *E* – CH₃OH lines, respectively.

⁴<http://physics.nist.gov/cgi-bin/micro/table5/start.pl>

⁵<https://cdms.astro.uni-koeln.de/cdms/portal>

⁶<https://spec.jpl.nasa.gov>

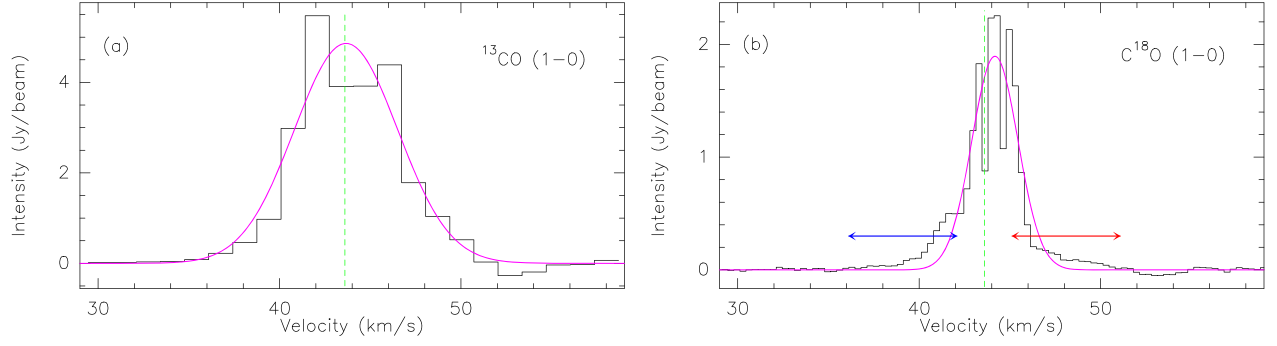


Figure 8. Low-resolution spectra of the $^{13}\text{CO}(1-0)$ and $\text{C}^{18}\text{O}(1-0)$ lines towards G19.88-0.53. The area over which the spectra are extracted covers all the cores. The vertical green line denotes the LSR velocity, 43.6 km s^{-1} . The red and blue arrows in (b) spans the range over which the integrated intensity map is constructed to trace the outflow wings (discussed in Section 4.3.2).

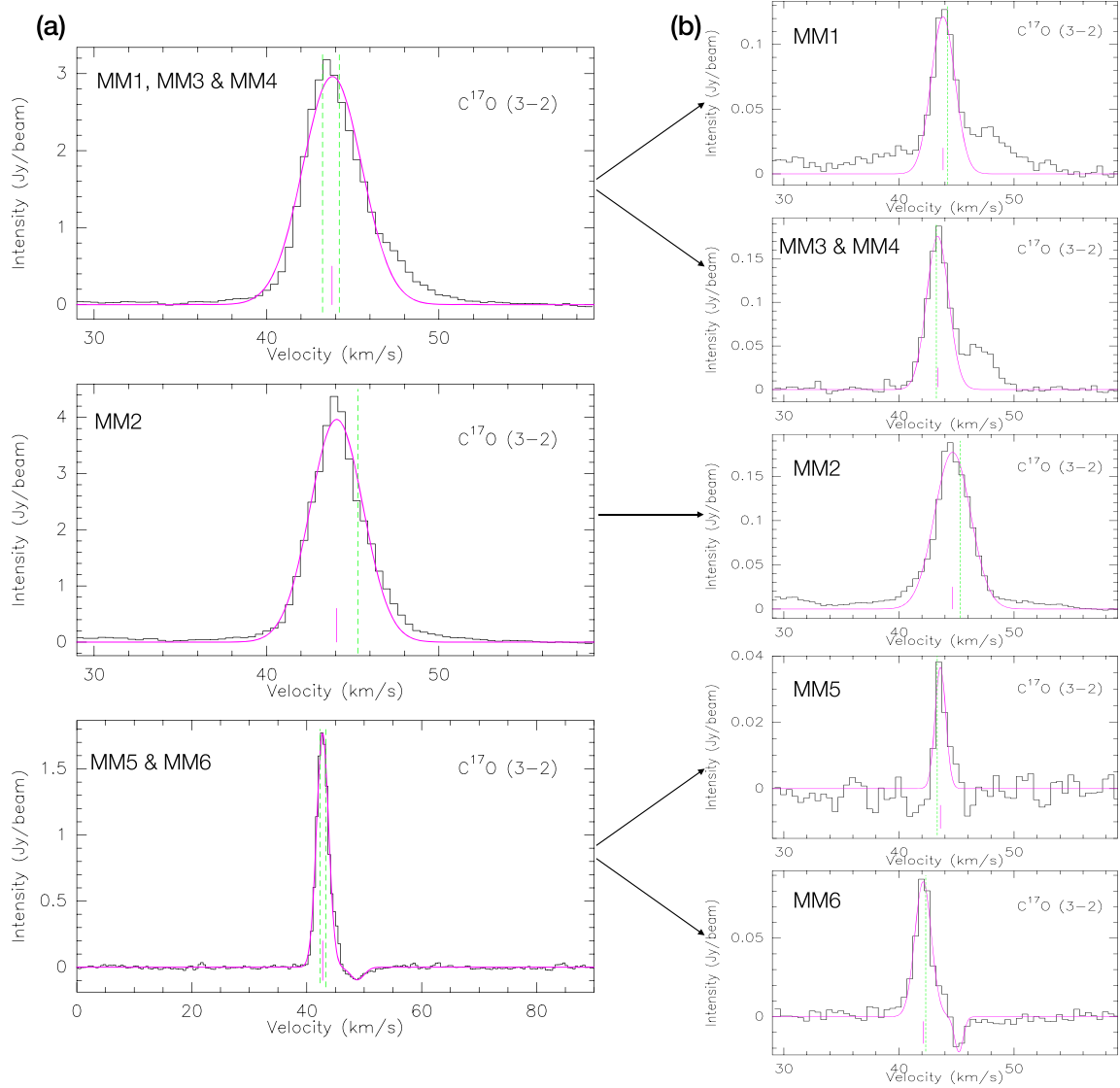


Figure 9. The $J = 3 - 2$ transition of C^{17}O towards the mm cores associated with G19.88-0.53 from the (a) low-resolution ($5.2 \text{ arcsec} \times 2.6 \text{ arcsec}$) data averaged over the beam and (b) high-resolution ($0.67 \text{ arcsec} \times 0.47 \text{ arcsec}$) data averaged over a region covering each core. The magenta curve represents the best fit to each spectrum. Double Gaussians are used to fit the spectra towards MM5 and MM6 (low resolution) and MM6 (high resolution). The dashed green line denotes the LSR velocity of each core. The magenta lines in the spectra mark the emission peaks.

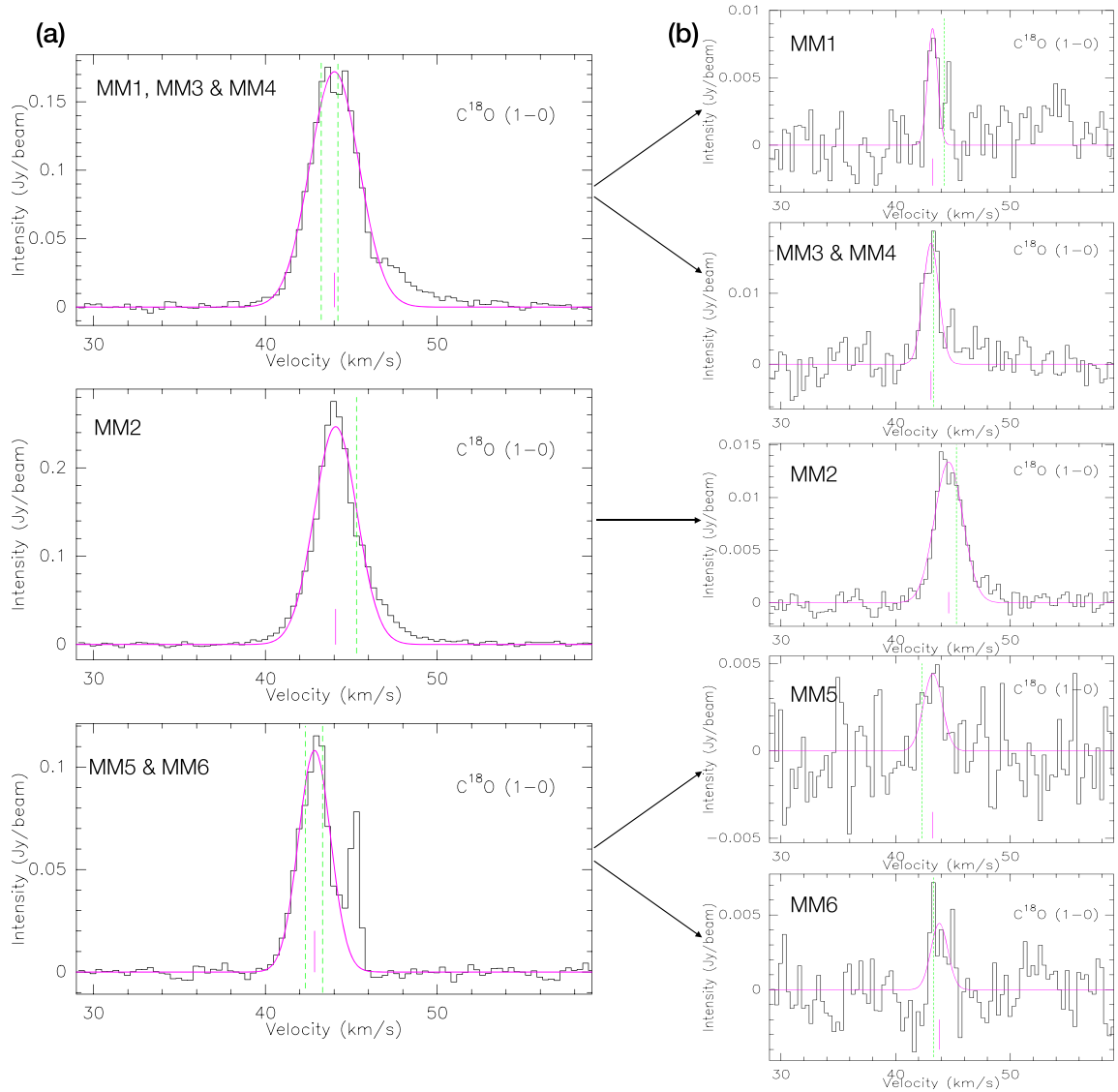


Figure 10. Same as Fig. 9 for the $C^{18}O$ (1 – 0) transition detected towards the mm cores associated with G19.88-0.53 from the (a) medium-resolution (2.6 arcsec \times 2.2 arcsec) data extracted over the same region as in Figs 9(a) and (b) high-resolution (0.46 arcsec \times 0.28 arcsec) data averaged over a region covering each core.

derived for the cores. In case of the $C^{17}O$ (3 – 2) line, spectra from the lower resolution Band 7 data cube are extracted over the beam area covering three regions (1) MM1, MM3, and MM4 (2) MM2, and (3) MM5 and MM6 and shown in Fig. 9(a). Region (1), covering MM1, MM3, and MM4, shows a clear red wing. However, for region (2), probing MM2, the wing is not very prominent. In case of region (3), an inverse P-Cygni profile is seen. A double Gaussian is used to fit this profile. Fig. 9(b) shows the high-resolution spectra of this line. As discussed earlier, since the separation between MM3 and MM4 is less than the beam size, the spectrum is extracted over a region covering both cores. Given the signal-to-noise ratio of the high-resolution spectra for MM1, MM3, and MM4, it is difficult to interpret the second red-shifted peaks seen as genuine additional components. These features are mostly broad outflow wings. Core MM6 displays a distinct inverse P-Cygni profile and is fitted by a double Gaussian.

Medium resolution $C^{18}O$ (1 – 0) line spectra extracted over the same three regions used for the $C^{17}O$ (3 – 2) spectra are plotted in

Fig. 10(a) with the high-resolution spectra presented in Fig. 10(b). Similar features are seen though the signal-to-noise of the high-resolution spectra, especially for MM5 and MM6, is poor compared to that of the $C^{17}O$ (3 – 2) line spectra. Also, the medium resolution combined spectrum for MM5 and MM6 shows an additional red-shifted narrow component that is difficult to understand. This component is, however, not detected in the high-resolution spectrum extracted over the same region, and hence could possibly be an artefact. Line parameters for the three transitions of CO determined by fitting Gaussian profiles using CLASS90 are listed in Table 6.

4 DISCUSSION

4.1 Ionized jet

Given that G19.88-0.53 is classified as an EGO, and hence likely associated with a jet/outflow, we are prompted to investigate the nature of the associated radio emission. As seen in Fig. 2(b),

Table 6. Parameters of the isotopologues of the CO molecule detected towards G19.88-0.53 from spectral data cubes at different spatial resolutions. The LSR velocity (V_{LSR}), line width (ΔV), intensity and velocity integrated intensity ($\int I_\nu dV$) of each transition are obtained from the single or double Gaussian profiles fits to the extracted spectra.

Core	V_{LSR} (km s $^{-1}$)	ΔV (km s $^{-1}$)	Intensity (Jy beam $^{-1}$)	$\int I_\nu dV$ (Jy beam $^{-1}$ km s $^{-1}$)
$^{13}\text{CO}(1-0)$				
Low-resolution (16.9 arcsec \times 8.0 arcsec)				
MM1-MM6	43.7	6.7	4.9	34.8
$\text{C}^{17}\text{O}(3-2)$				
Low-resolution (5.2 arcsec \times 2.6 arcsec)				
MM1, MM3, and MM4	43.8	4.0	3.0	12.7
MM2	44.1	3.6	4.0	15.3
MM5 and MM6	42.8 (B)	2.5 (B)	1.8 (B)	4.6 (B)
	48.8 (R)	2.8 (R)	-0.1 (R)	-0.3 (R)
High-resolution (0.67 arcsec \times 0.47 arcsec)				
MM1	43.8	2.4	0.1	0.3
MM2	44.7	3.7	0.2	0.7
MM3 and MM4	43.4	2.3	0.2	0.4
MM5	43.6	1.1	0.04	0.04
MM6	42.1 (B)	1.7 (B)	0.09 (B)	0.2 (B)
	45.2 (R)	0.9 (R)	-0.02 (R)	-0.02 (R)
$\text{C}^{18}\text{O}(1-0)$				
Low-resolution (16.9 arcsec \times 8.0 arcsec)				
MM1-MM6	44.2	3.0	1.9	6.0
Medium-resolution (2.6 arcsec \times 2.2 arcsec)				
MM1, MM3 & MM4	44.0	3.4	0.2	0.6
MM2	44.1	2.9	0.2	0.8
MM5 & MM6	42.9	2.2	0.1	0.3
High-resolution (0.46 arcsec \times 0.28 arcsec)				
MM1	43.2	1.0	0.01	0.01
MM2	44.6	2.9	0.01	0.04
MM3 & MM4	43.1	1.6	0.02	0.03
MM5	43.8	1.7	0.004	0.01
MM6	43.2	1.9	0.004	0.01

the ionized emission associated with G19.88-0.53 exhibits a linear morphology consisting of the components R1 and R2 in the east–west direction. The radio emission from both the components is weak (~ 0.2 mJy), and they are located towards the centroid of a large scale (~ 1 arcmin) molecular outflow (Fig. 15a, Section 4.3.2). These traits are in agreement with the typical observational features expected in ionized jets (Anglada 1996; Rodríguez 1997; Purser et al. 2016; Rosero et al. 2019; Obonyo et al. 2019).

The spectral index is a crucial parameter that helps in understanding the nature of the radiation mechanism. This is defined as $S_\nu \propto \nu^\alpha$, where, S_ν is the flux density at frequency ν . As discussed in Section 3.1, G19.88-0.53 is not detected in Band 4. Further, weak emission in Band 5 would render the in-band spectral index estimation highly unreliable as has also been discussed by Rosero et al. (2016). Emission at 1391.6 MHz encompasses the component IRAS 18264-1152b. This makes it possible to use this uGMRT sub-band and VLA maps from Zapata et al. (2006) to derive the spectral index of R1. An accurate determination of the spectral index requires same spatial scales to be probed at the frequencies used. The synthesized beam sizes of uGMRT 1391.6 MHz and VLA 8 GHz (3.6 cm) maps are nearly identical indicating similar uv coverage and hence similar spatial scales probed. This is not the case for the 1.3 cm data. For this, we convolve the map to the match the resolution of the other two frequencies. The radio SED is shown in Fig. 11. For 651.4 MHz, we obtain an upper limit for the flux density (rms of the map), which is shown in the plot. For the VLA maps, we use the peak flux density as well. The fit to the radio SED of component

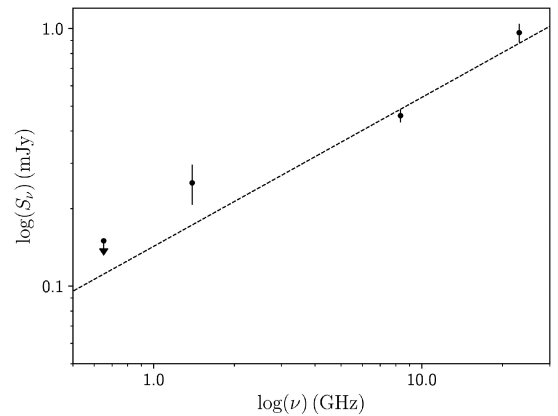


Figure 11. Radio SED for component R1 (IRAS 18264-1152b) using the data points at 1391.6 MHz, 8 GHz (3.6 cm) and 23 GHz (1.3 cm). At 651.4 MHz, an upper limit for the flux density is given. The straight line gives the linear fit with spectral index estimate of 0.58 ± 0.19 .

R1 (IRAS 18264-1152b) yields a spectral index value of 0.58 ± 0.19 that corroborates well with radio continuum emission originating due to the thermal free–free emission from an ionized collimated stellar wind (and references therein Rosero et al. 2019). For component R2, similar analysis of spectral index estimation is not possible given that this component is not detected in the VLA maps of Zapata et al. (2006).

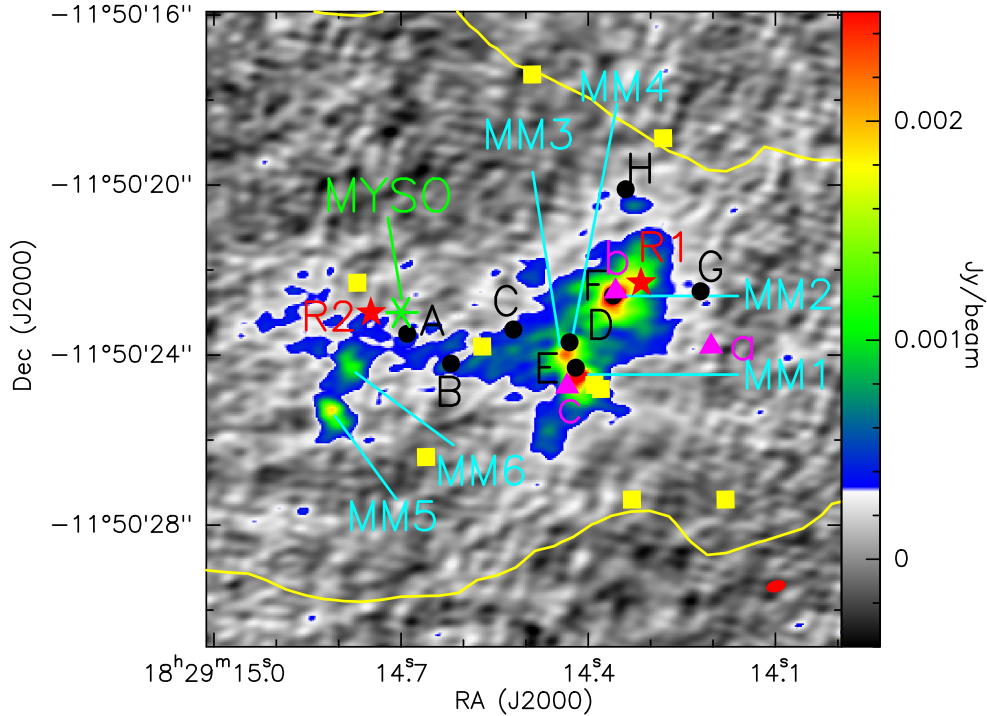


Figure 12. Multifrequency picture of the various components of the protocluster. The *ALMA* 2.7 mm map is depicted in the colour scale. The yellow contour traces the 3σ level of the $4.5\ \mu\text{m}$ emission. The red stars mark the positions of the radio components R1 and R2 from the uGMRT map. The black-filled circles indicate the positions of the radio sources identified by Rosero et al. (2016). The magenta triangles represent the radio components from Zapata et al. (2006). The position of the MYSO associated with G19.88-0.53 is indicated with ‘*’. The filled yellow squares are the 44 GHz methanol masers spots in the vicinity of G19.88-0.53 identified by Rodríguez-Garza et al. (2017).

The spectral index estimation of R1 obtained from the combination of uGMRT and VLA maps of Zapata et al. (2006) is in excellent agreement with value of 0.6 ± 0.1 derived by Rosero et al. (2016) using flux densities at four central frequencies (4.9 and 7.4 GHz at 6 cm and 20.9 and 25.5 GHz at 1.3 cm). In comparison, Zapata et al. (2006) obtain a lower value of 0.27 ± 0.06 . The 3.6 cm flux density of IRAS 18264-1152b used by these authors would also include emission from IRAS 18264-1152a and IRAS 18264-1152c thus rendering a shallower slope. Based on the weak emission, elongated morphology, association with molecular outflows and rising spectral index values, the radio emission favours shock ionization over the H II region picture. Hence, Rosero et al. (2019) list source F (R1) as an ionized jet/wind candidate. Inference of a likely thermal jet or a partially optically thick H II region is drawn by Zapata et al. (2006) as well. The identification of R1 as a thermal jet is well supported by the detection of several shock-excited H_2 lines in the UKIRT-NIR spectra of G19.88-0.53 presented in Section 3.2. To the best of our knowledge, this is the first detection of the ionized jet associated with G19.88-0.53 at the lower frequency regime of uGMRT. Similar result is obtained by our group for EGO G12.42 + 0.50 (Issac et al. 2019). The authors propose the coexistence of a thermal jet and a UC H II region driven by the same MYSO to explain the observed radio, mm, and IR emission for G12.42 + 0.50.

4.2 A protocluster revealed

EGO G19.88-0.53 has been proposed as an outflow powered by a MYSO (De Buizer & Vacca 2010) and a multiple outflow source (Varricatt et al. 2010). Several studies (e.g. Cyganowski, Brogan &

Hunter 2007; Cyganowski et al. 2011) have shown that MYSOs are actually protoclusters harbouring protostars with different masses and in various stages of evolution. Given the predilection of high-mass stars to form in clustered environments, it is likely that EGOs, in fact harbour protoclusters rather than single high-mass stars. Based on SOFIA FORCAST imaging and archival infrared data of 12 EGOs, Towner et al. (2019) suggest the number of massive sources per EGO to be between 0.9 and 1.9. Similar inferences have been drawn from studies towards other identified EGOs (e.g. Brogan et al. 2011; Cyganowski et al. 2012).

The 870 μm clump cocoons the EGO G19.88-0.53 where the extended $4.5\ \mu\text{m}$ emission lies towards the centre as is seen in Fig. 5(a). In Fig. 12, we present the various radio and mm sources associated with this EGO. The 2.7 mm dust emission, with the cluster of detected cores lie deeply embedded within the $4.5\ \mu\text{m}$ emission. Portion of the 3σ contour of the $4.5\ \mu\text{m}$ emission is seen in the region displayed in the figure. Within the dust emission lie the two radio components R1 and R2 mapped at 1391.6 MHz with uGMRT. As discussed in the previous section, R1 (VLA source F) is most likely an ionized thermal jet. Regarding component R2 (VLA source A) and the other six compact VLA sources (B, C, D, E, G, and H) located within the EGO, Rosero et al. (2016) discuss the likelihood of them being H II regions around rapidly accreting massive stars that quench the UV photons thus giving rise to weak radio sources. They also keep alive the debate of these being ionized jets instead. Zapata et al. (2006) also suggest that the component IRAS 18264-1152c (VLA source E) is likely to be an optically thick H II region. These authors detect an additional component IRAS 18264-1152a of similar nature taking the number of distinct radio sources to be nine. Furthermore, from the analysis of *ALMA* 2.7 mm high-resolution continuum map,

Table 7. Identified radio and mm components of the protocluster associated with G19.88-0.53.

Compact radio sources VLA ^a	Radio components VLA ^b	Radio components uGMRT 1391.6 MHz ^c	Millimetre cores ALMA 2.7 mm ^c	Remark
A	–	R2	–	MYSO ^d /Ionized jet
B	–	–	–	UCH II/Ionized jet
C	–	–	–	UCH II/Ionized jet
D	–	–	MM3 & MM4	UCH II/Ionized jet
E	IRAS 18264-1152c	–	MM1	UCH II/Ionized jet
F	IRAS 18264-1152b	R1	MM2	Ionized jet
G	–	–	–	UCH II/Ionized jet
H	–	–	–	UCH II/Ionized jet
–	IRAS 18264-1152a	–	–	UCH II/Ionized jet
–	–	–	MM5	Dense core
–	–	–	MM6	Dense core

^aRosero et al. (2016). ^bZapata et al. (2006). ^cThis work. ^dDe Buizer & Vacca (2010).

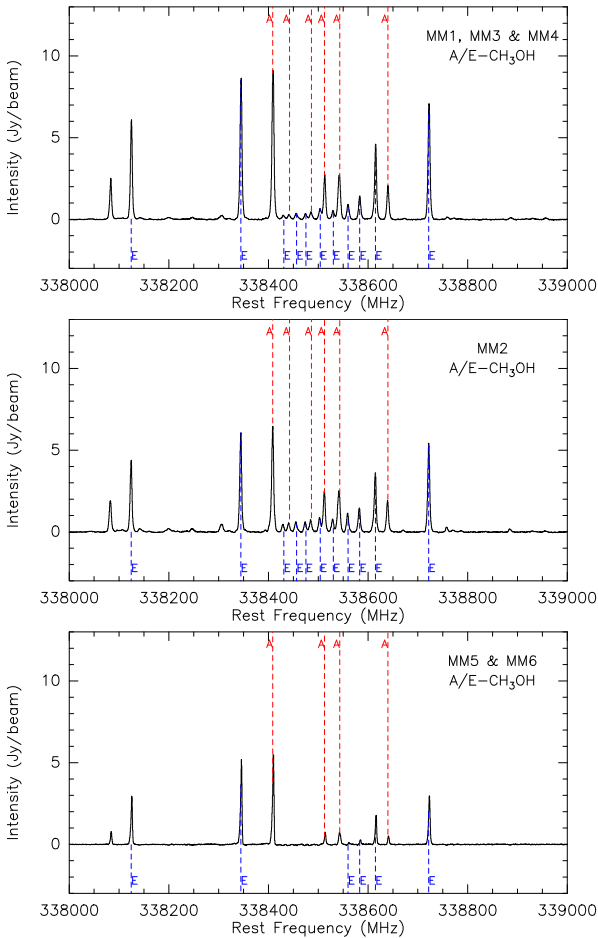


Figure 13. Spectra of the $A/E - \text{CH}_3\text{OH}$ lines detected towards G19.88-0.53 extracted over three regions from the low-resolution Band 7 spectral cube. The top panel is the spectrum extracted over the region covering MM1, MM3, and MM4, middle panel corresponds to MM2 and the bottom panel is over the region covering MM5 and MM6. The dashed red and blue lines indicate the peak positions of the $A - \text{CH}_3\text{OH}$ and $E - \text{CH}_3\text{OH}$ lines, respectively.

we discover six compact cores located within the EGO. Table 7 lists the radio and mm sources and their cross-identification.

Given the detection of several radio components and mm cores, the picture of a protocluster with multiple (11) members is clearly

perceivable. The observational signatures of the members show clear evidence of different evolutionary phases. However, high-sensitivity radio surveys of ionized jets have shown association with extended lobes and string of radio knots (e.g. Garay et al. 2003; Guzmán, Garay & Brooks 2010; Purser et al. 2016; Hofner et al. 2017). From the alignment of the radio sources B, C and F, and the spectral index of F, one can visualize a similar scenario. It is thus plausible that we are probing a string of knots of a single ionized jet driven by R1/MM2/F. Similarly, the components A and G could be part of this jet system though the possibility of another jet driven by R2/MYSO/A cannot be ruled out. If these radio components are indeed knots/lobes of the identified jet systems, then the number of distinct members of the detected protocluster would be less than 11. Further studies are required to interpret the exact nature the compact radio sources.

4.2.1 CH_3OH rotational temperature

Molecular line transitions can be used to analyse the core properties. As seen in Fig. 7, multiple transitions of CH_3OH are detected towards the mm cores associated with G19.88-0.53. This motivates us to use rotational temperature diagram (RTD; also referred to as Boltzman diagram) to estimate the rotational temperature and the beam averaged column density of the identified mm cores. To generate the RTDs, we use the low-resolution ($5.3\text{arcsec} \times 2.6\text{arcsec}$) ALMA data cubes. Given the beam size, we extract the spectrum covering three regions (1) MM1, MM3, and MM4, (2) MM2, and (3) MM5 and MM6. The retrieved spectra are shown in Fig. 13 and the line parameters are listed in Tables A2, A3, and A4. The detected methanol lines have linewidths of several km s^{-1} and none show unusually high line intensities. Thus, these are unlikely to be associated with maser excitations.

Considering the molecular emission to be optically thin, the column density of the upper level, N_u can be computed from the integrated line intensity following the expression:

$$N_u = \frac{8\pi k \nu^2}{hc^3 A_u} \int I_\nu (\text{Jy beam}^{-1}) dV (\text{km s}^{-1}) / \eta_{\text{bf}}, \quad (1)$$

where A_u is Einstein coefficient and η_{bf} is the beam-filling factor, taken to be 1 since the emission region is larger than the beam size (Ren et al. 2012). Further, under conditions of local thermodynamic equilibrium, the measured line intensities are proportional to the level populations that are characterized by a single rotational temperature. The rotational temperature, T_{rot} , and the beam averaged column density, N_T , can be determined using the expression (Blake et al.

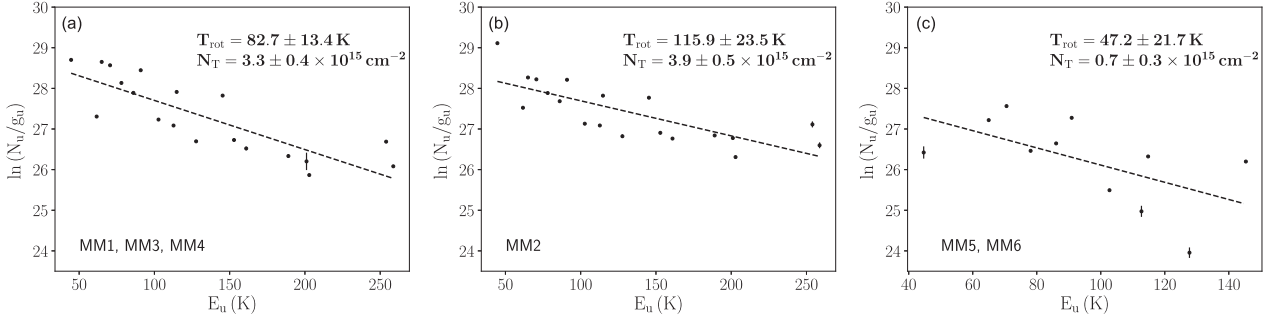


Figure 14. The rotational temperature diagram of the CH₃OH lines at the mm cores, MM1 through MM6 towards G19.88-0.53. The circles indicate the data points with 3 σ error bars. The linear least-squares fit is indicated by the dashed line.

Table 8. Derived parameters of the mm cores associated with G19.88-0.53.

Core	Radius (10 ⁻³ pc)	T_{rot} (K)	N_T (10 ¹⁵ cm ⁻²)	$N_T/N(\text{H}_2)$ (10 ⁻⁷)	Mass $_{T_{\text{rot}}}$ (M_{\odot})	$n(\text{H}_2)$ (10 ⁸ cm ⁻³)
MM1	5.4	82.7 ± 13.4	3.3 ± 0.4	0.6	14.5	3.2
MM2	10.1	115.9 ± 23.5	3.9 ± 0.5	0.7	29.6	1.0
MM3 & MM4	6.6	82.7 ± 13.4	3.3 ± 0.4	0.6	16.1	1.9
MM5	5.2	47.2 ± 21.7	0.7 ± 0.3	0.1	13.1	3.2
MM6	5.3	47.2 ± 21.7	0.7 ± 0.3	0.1	9.5	2.2

1987; Liu et al. 2002; Remijan et al. 2004)

$$\ln\left(\frac{N_u}{g_u}\right) = \ln\left(\frac{N_T}{Q_{\text{rot}}}\right) - \frac{E_u}{T_{\text{rot}}}$$

$$= \ln\left[2.04 \times 10^{20} \frac{\int I_\nu (\text{Jy beam}^{-1}) dV (\text{km s}^{-1})}{\theta_a \theta_b (\text{arcsec}^2) \nu^3 (\text{GHz}) S \mu^2 (\text{debye}^2)}\right], \quad (2)$$

where N_u , g_u and E_u are the upper level column density, rotational degeneracy factor, and energy, respectively, $Q_{\text{rot}} (= 1.23 T_{\text{rot}}^{1.5})$ is the rotational partition function (Remijan et al. 2004; Ren et al. 2012), θ_a and θ_b are the beam sizes, ν is the rest frequency, S is the line strength, μ is the dipole moment, and the integration of I_ν over velocity, V , is the integrated line intensity. Values for E_u and $S\mu^2$ for detected transitions are retrieved from *splatalogue – data base for astronomical spectroscopy*⁷ and compiled in Table A1. The generated RTDs towards the mm cores are plotted in Fig. 14. Linear least-square fits to the data points gives the estimate of the rotational temperature, T_{rot} and the beam averaged column density, N_T of the cores and are listed in Table 8. For cores MM1, MM3, and MM4, the estimates would be an average value of the three clumps as is the case with the estimates for MM5 and MM6. Estimated values of T_{rot} and N_T lie in the range ~ 47 –116 K and ~ 0.7 –4 $\times 10^{15}$ cm⁻², respectively, with core MM2 being the hottest with a rotational temperature of 115.9 K. The rotational temperatures for the cores are greater than the average cold dust temperature of 18.6 K deduced for the dust clump (Section 3.3.1). The difference in these temperatures could be that the CH₃OH emission arises from the hot cores. The gas and dust could also be thermally decoupled and the higher rotational temperatures could be the result of enhanced collisional excitations of the molecular gas by shocks in the outflow region. A large scatter is seen in the combined RTD of MM5 and MM6 possibly indicating more than one temperature components. However, higher resolution and better signal-to-noise ratio data are required to address this.

To examine the assumption of optically thin transitions, we derived the optical depth of the CH₃OH lines adopting the following expression from Ren et al. (2012):

$$\tau = \frac{c^3 \sqrt{4 \ln 2}}{8 \pi \nu^3 \sqrt{\pi} \Delta V} N_u A_u \left[\exp\left(\frac{h \nu}{k T_{\text{rot}}}\right) - 1 \right]. \quad (3)$$

The estimated values are listed in Table A2, A3, and A4. Only two transitions for the combined cores of MM1, MM3, and MM4 show values ~ 0.1 . Rest of the lines are far more optically thin. Considering T_d (18.6 K) instead of T_{rot} , to account for temperature uncertainties, if any, also gives optically thin estimates for the transitions. In case of optically thick lines, effects of optical depth can be taken into account by multiplying the term N_u/g_u with a correction factor $C_\tau = \tau/(1 - e^{-\tau})$ and subsequently fitting for the rotational temperature iteratively (Ren et al. 2012). We also estimate the relative abundance of CH₃OH with respect to the H₂ molecule and tabulate the values in Table 8 along with the H₂ number density.

Menten et al. (1986), in their study of *E*-type methanol lines towards a few Galactic molecular line sources concluded that these lines originate from hot clumps embedded in the molecular gas and have densities $\sim 10^6$ – 10^7 cm⁻³, temperatures ~ 100 K, and sizes ~ 1 pc. The abundance relative to the H₂ molecule was found to be in the range of 10^{-7} – 10^{-6} . In another study of molecular clouds, Leurini et al. (2007) study the early phases of high-mass stars, particularly the protostellar objects and IRDCs, using methanol as a diagnostic tool. In their study, they discuss on the origin of CH₃OH lines that arise from the different components of the protostellar object, which includes the overall emission from the clump and the dense, hot core. In some cases contribution of outflow emission is also included. Temperatures, densities, and abundances fall in the range of 17–36 K, 2×10^5 – 3×10^6 cm⁻³, and 7×10^{-10} – 2×10^{-8} , respectively, if the molecular transition occurs from the bulk emission of the clump. The range changes to 60–300 K, $\gtrsim 10^6$ cm⁻³, and $\gtrsim 10^{-7}$, respectively, for hot cores. The estimated values for cores associated with G19.88-0.53 indicates the origin of the CH₃OH emission from hot cores, especially for MM1–MM4.

⁷<http://www.cv.nrao.edu/php/splat/>

4.2.2 Nature of mm cores

To decipher the nature of the mm cores, we estimate the masses. This is done following the formalism described in Cheng et al. (2018). Assuming optically thin emission, the core masses can be expressed as

$$M = 0.0417 M_{\odot} \left(e^{0.533(\lambda/1.3 \text{ mm})^{-1}(T/20 \text{ K})^{-1}} - 1 \right) \left(\frac{F_{\nu}}{\text{mJy}} \right) \times \left(\frac{\kappa_{\nu}}{0.00638 \text{ cm}^2 \text{ g}^{-1}} \right)^{-1} \left(\frac{d}{2.4 \text{ kpc}} \right)^2 \left(\frac{\lambda}{1.3 \text{ mm}} \right)^3, \quad (4)$$

where the opacity

$$\kappa_{\nu} = 0.1(\nu/1000 \text{ GHz})^{\beta} \text{ cm}^2 \text{ g}^{-1} \quad (5)$$

with β , the dust emissivity spectral index, fixed at 2.0 is the same as used for modelling the FIR SED. F_{ν} is the integrated flux density of each component, d is the distance to the source, and λ is the wavelength taken as 2.7 mm. Since we do not have the information of dust temperatures at the dense core scales, we use the estimated T_{rot} values in the above expression to derive masses. Compared to the average dust temperature of the clump, these temperatures would be a better choice to represent the hot cores. The mass estimates range between 10 and 30 M_{\odot} and are listed in Table 8. Angular sizes given in Table 5 are converted to linear sizes and listed in the table. From the estimated masses and sizes, the detected cores satisfy the criterion, $m(r) > 870 M_{\odot} (r/\text{pc})^{1.33}$ (Kauffmann et al. 2010) and qualify as high-mass star-forming cores. In comparison to the numbers discussed by Towner et al. (2019), we detect as many as 11 possible distinct massive components in the G19.88-0.53 protocluster that include MYSOs driving ionized jets/outflows and UCH II regions.

4.3 Kinematics of the protocluster G19.88-0.53

4.3.1 Infall signature in MM6

As discussed in Section 3.4, CO transitions from higher energy levels are likely tracers of the inner parts of molecular clouds. The $\text{C}^{17}\text{O}(3-2)$ molecular transition shows an inverse P-Cygni profile for core MM6. Inverse P-Cygni profiles are generally considered as evidence of gas infall (Wu et al. 2009; Liu, Wu & Zhang 2013). In such profiles, the redshifted absorption feature originates from the dense gas along the line of sight and located towards the near side of the observer and moving away. The emission component is due to the gas on the far side of the central source with its motion towards the observer. Although several studies have attributed the presence of an inverse P-Cygni or redshifted absorption profile to possible gas inflow to the central core (e.g. Keto, Ho & Reid 1987; Qin et al. 2008; Zapata et al. 2008; Liu et al. 2013; Liu, Wu & Zhang 2013), detailed investigations of inverse P-Cygni profiles of CO lines in high-mass star-forming regions are fairly limited (e.g. Wu et al. 2009; Beltrán et al. 2011; Klaassen et al. 2011).

We use the $\text{C}^{17}\text{O}(3-2)$ line profile to estimate the infall velocity and the mass infall rate of the compact core, MM6 associated with G19.88-0.53. The infall velocity is estimated as $V_{\text{inf}} = |V_{\text{LSR}} - V_{\text{R}}|$ (Beltrán et al. 2011), where V_{R} is the peak of the redshifted absorption. From the infall velocity, the mass infall rate is determined following the expression $\dot{M}_{\text{inf}} = 4\pi R^2 V_{\text{inf}} \rho$ (López-Sepulcre, Cesaroni & Walmsley 2010), where ρ is the average volume density of the cores, given by $\rho = M/\frac{4}{3}\pi R^3$. From the estimated core mass and radius, the infall velocity and mass infall rate are calculated to be 2.9 km s^{-1} and $16.1 \times 10^{-3} M_{\odot} \text{ yr}^{-1}$, respectively, and listed in Table 9. The

Table 9. The infall velocity, V_{inf} , and mass infall rate, \dot{M}_{inf} , of core MM6 associated with G19.88-0.53, estimated using the $\text{C}^{17}\text{O}(3-2)$ line.

Core	V_{LSR} (km s^{-1})	V_{R} (km s^{-1})	V_{inf} (km s^{-1})	\dot{M}_{inf} ($10^{-3} M_{\odot} \text{ yr}^{-1}$)
MM6	42.3	45.2	2.9	16.1

infall velocity and mass infall rate are consistent with the typical values of several km s^{-1} and $\sim 10^{-3}$ – $10^{-2} M_{\odot} \text{ yr}^{-1}$, respectively, found towards hot molecular cores (Liu, Wu & Zhang 2013).

4.3.2 Outflow activity

Co-existing with ionized jets, molecular outflows are ubiquitous in active star-forming cores (e.g. Beuther et al. 2002b; Purser et al. 2016). These outflows are understood to be driven by the jets that entrain the gas and dust from the surrounding clump. Based on a large number of studies, broad wings of CO lines are accepted as signatures of molecular outflow (Beuther et al. 2002b; Qiu et al. 2009). The detection of the isotopologues of CO towards G19.88-0.53 enables us to investigate the associated outflow(s). Towards this, we construct the zeroth moment map of the $\text{C}^{18}\text{O}(1-0)$ emission from the low-resolution cube using the CASA task, IMMOMENTS. The velocity range to integrate is estimated from the extracted spectra discussed earlier and shown in Fig. 8(b). Following Sanna et al. (2014) and Issac et al. (2019), we define the inner limits of the velocity at $\sim V_{\text{LSR}} \pm \text{FWHM}/2$, where FWHM is the C^{18}O linewidth. Thus, for the blue wing, the emission is integrated over the velocity range of 36.1–42.1 km s^{-1} . Similarly, for the red wing the integration is done from 45.1 to 51.1 km s^{-1} . The spatial extent and morphology of the outflow is revealed in Fig. 15(a). To facilitate morphological correlation of the outflow with the EGO, the contours of the blue and red lobes are overlaid on the *Spitzer* IRAC colour composite image. The magenta ellipses denote the location of the H_2 knots identified by Lee et al. (2012) and Varricatt et al. (2010) from the continuum-subtracted H_2 image. Two distinct and spatially separated outflow lobes in the north-east and south-west direction are identified with the central part of G19.88-0.53 located towards the centroid of the outflow. The direction and location of the blue lobe is towards MHOs 2203 and 2205. In their survey of massive molecular outflows in high-mass star-forming regions using the $^{12}\text{CO}(2-1)$ transition, Beuther et al. (2002b) discuss the detection of a bipolar CO outflow towards the infrared source, IRAS 18264-1152, associated with G19.88-0.53. The orientation is consistent with that seen in Fig. 15(a).

The figure also shows the 2.7 mm emission outlined by the black contour. A zoomed-in picture of the 2.7 mm map covering the central part of the extended green emission is displayed in Figs 15(b) and (c). We investigate outflow signatures in the high-resolution $\text{C}^{17}\text{O}(3-2)$ and $\text{C}^{18}\text{O}(1-0)$ emission in Bands 7 and 3 cubes, respectively. From a visual inspection of the outflow wings seen in the spectra presented in Fig. 9, the moment zero maps of the $\text{C}^{17}\text{O}(3-2)$ over the velocity ranges 36.1–42.1 km s^{-1} and 45.1–51.1 km s^{-1} are constructed. The contours of the moment zero maps are overlaid in Fig. 15(b). Similarly, for the $\text{C}^{18}\text{O}(1-0)$ emission, the moment zero maps are built over the velocity ranges 41.6–43.6 km s^{-1} and 43.6–45.6 km s^{-1} , the contours of which are overlaid on Fig. 15(c). Since the high-resolution $\text{C}^{18}\text{O}(1-0)$ data have poor signal-to-noise ratio in comparison to the high-resolution $\text{C}^{17}\text{O}(3-2)$, no emission was detected above the noise beyond the outer limits, 41.6 and 45.6 km s^{-1} of the blue and red lobes, respectively. Interestingly, from the contours of the moment zero maps overlaid in Figs 15(b)

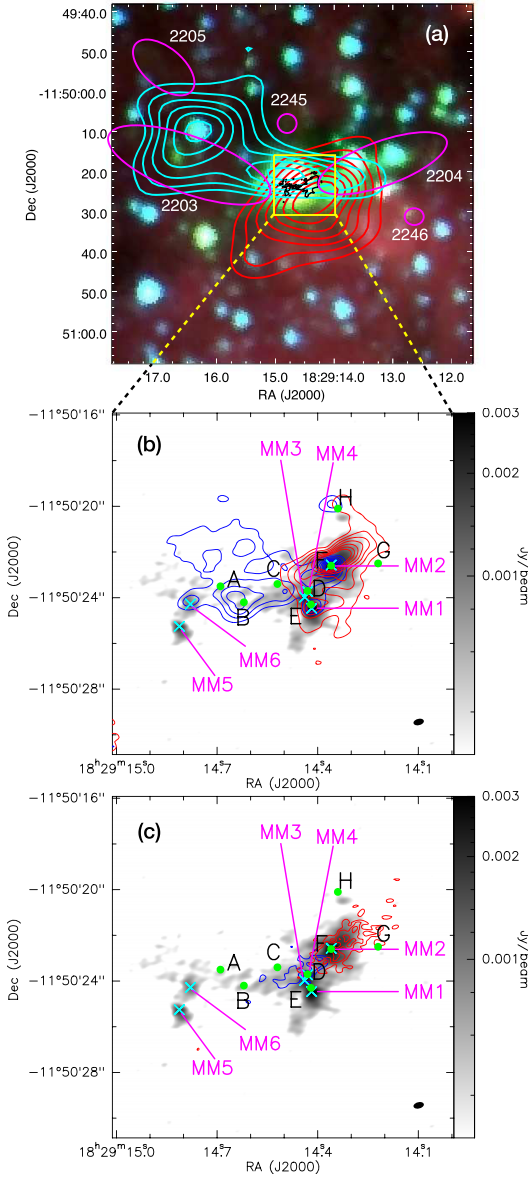


Figure 15. (a) The *Spitzer* IRAC colour composite image of G19.88-0.53 with the 3σ ($\sigma = 0.12 \text{ mJy beam}^{-1}$) *ALMA* 2.7 mm emission contours in black. The moment zero map from the low-resolution data of the C¹⁸O(1-0) line integrated from 36.1 to 42.1 km s⁻¹ and from 45.1 to 51.1 km s⁻¹ are represented using the blue and red contours, respectively. The contours start from the 3σ level for both the blue and red lobes and increase in steps of 2σ [$\sigma = 0.1$ (blue); $0.2 \text{ Jy beam}^{-1} \text{ km s}^{-1}$ (red)]. The magenta ellipses denote the location of the H₂ knots identified by Lee et al. (2012) and Varricatt et al. (2010). (b) The 2.7 mm emission is depicted in the grey scale. The positions of the mm cores are marked using 'x's. The moment zero map from the high-resolution data of C¹⁷O(3-2) line over the velocity ranges 36.1–42.1 km s⁻¹ and 45.1–51.1 km s⁻¹, covering the blue and red lobes are illustrated in blue and red contours, respectively. The contours start from 5σ level for both lobes and increase in steps of 4σ ($\sigma = 16.2 \text{ mJy beam}^{-1} \text{ km s}^{-1}$). The filled circles correspond to the radio sources detected by Rosero et al. (2016). (c) Same as (b) for the high-resolution C¹⁸O(1-0) line integrated over the velocity ranges 41.6–43.6 km s⁻¹ and 43.6–45.6 km s⁻¹ covering the blue and red lobes, respectively. The contours start from 3σ level for both lobes and increase in steps of 1σ ($\sigma = 7.7 \text{ mJy beam}^{-1} \text{ km s}^{-1}$).

and (c), the high-resolution data traces another relatively collimated outflow in the south-east and north-west direction with core MM2 located in the close vicinity of its centroid.

To delve further, we generate channel maps of the high-resolution C¹⁸O(1-0) transition shown in Fig. 16. The emission in the velocity range 41.6–43.6 km s⁻¹ is elongated towards south-east of core MM2, whereas the emission with velocities 44.6–45.6 km s⁻¹, the elongation is towards north-west of MM2 thus giving clear indication of the presence of an outflow. Close to the LSR velocity of the MM2 (44.6 km s⁻¹), as expected, there is overlap of emission from the blue and the red components. The small projected velocities seen is possibly due to the effect of small inclination angle.

Using the high-resolution SiO(2-1) emission, Qiu et al. (2007) detected the presence of two quasi-perpendicular collimated outflows, one in the south-east and north-west direction and one in the north-east direction. Our high-resolution ALMA map probes the central portion of the outflow presented in Qiu et al. (2007). A close visual scrutiny of the figures presented by these authors indicate that the south-east and north-west SiO outflow is aligned with the C¹⁷O(3-2) and C¹⁸O(1-0) outflows displayed in Figs 15(b) and (c). Comparison with the H₂ outflows and the MHOs show a possible alignment with MHO 2204. Further, the direction of north-east SiO(2-1) outflow is consistent with MHO 2245. SiO is believed to be an excellent tracer of collimated molecular jets and shocks in the interstellar molecular clouds because it is formed due to the sputtering of Si atoms from the grains due to fast shocks (Hatchell, Fuller & Millar 2001; Miettinen et al. 2006; López-Sepulcre et al. 2011). In studies of several massive star-forming regions, protostellar jets were revealed by SiO emission (e.g. Cesaroni et al. 1999; Codella et al. 2013; Leurini et al. 2013). From their study of the massive star formation region IRAS 19410 + 2336, Widmann et al. (2016) conclude that the SiO emission is possible from the high-velocity C-type or CJ-type shocks associated with protostellar jets. uGMRT results have identified an ionized jet with the core MM2 that is in excellent agreement with the collimated outflow from high-resolution C¹⁸O(1-0) transition and the co-spatial SiO outflow of Qiu et al. (2007). Several studies point to the possibility that the massive outflows are powered by mm sources (e.g. Beuther et al. 2002b; Marseille et al. 2008). From the spatial extent and the maximum velocity of the flow, the dynamical time-scale ($T_{\text{dyn}} = L_{\text{flow}}/v_{\text{max}}$) is estimated to be of the order of 10^4 yr which is typical of outflows originating from mm cores rather than UC H II regions (Shepherd et al. 1998; Shepherd, Testi & Stark 2003; Qiu et al. 2009). This lends crucial support to our conclusion of R1 (MM2) being an ionized jet.

Based on multiwavelength data, the results and discussion presented in this paper enable us to draw a comprehensive picture of the star-forming region associated with G19.88-0.53. The EGO, which is embedded in a massive cold clump within an IRDC, is unveiled to be a young and active protocluster harbouring several massive components in early evolutionary phases. In conjunction with ionized and H₂ jets, the kinematic picture reveals multiple molecular outflows driven by one or more members of the protocluster.

5 SUMMARY

From the multifrequency and multiphase study of the EGO, G19.88-0.53 an interesting picture of it being a protocluster is revealed with multiple components spanning a wide evolutionary spectrum from hot cores in accretion phase to cores driving multiple outflows to possible UC H II regions. The main results are summarized below:

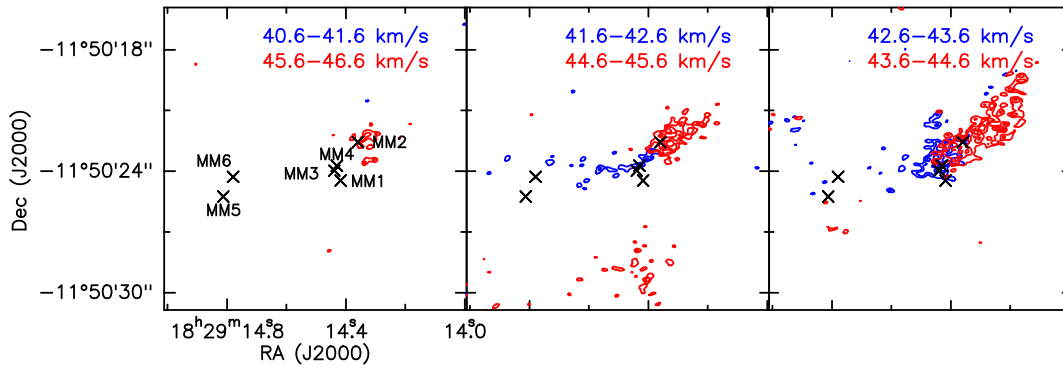


Figure 16. Channel maps of C^{18}O ($3-2$) line associated with G19.88-0.53 with a velocity resolution of 1 km s^{-1} from the high-resolution data. Each box contains a pair of maps corresponding to the red and blueshifted emissions at the same offset from the LSR velocity. Channel widths are indicated at the top left of each map. The contours start from the 3σ level of each map and increases in steps of 1σ . The positions of MM1, MM2, MM3, MM4, MM5, and MM6 are marked.

(i) G19.88-0.53 is located within a massive dust clump of mass $1911 M_{\odot}$, identified from the $870 \mu\text{m}$ map with the $4.5 \mu\text{m}$ emission towards its centre. Deeply embedded within this are nine distinct radio components and six dense mm cores unraveling a protocluster.

(ii) Deep uGMRT observations detect weak radio emission associated with G19.88-0.53. The radio continuum emission at 1391.6 MHz exhibits a linear structure consisting of two radio components, R1 and R2, in the east–west direction. The spectral index estimate of the radio component, R1, 0.58 ± 0.19 , confirms it as a thermal jet.

(iii) The shock-excited H_2 emission is established from the NIR spectroscopy in concordance with the jet/outflow scenario.

(iv) Six dense and compact dust cores (MM1–MM6) are identified from the high-resolution ALMA map at 2.7 mm map. The brightest of these cores, MM2, is coincident with the radio component R1. Based on the mass and size estimates, the cores qualify as high-mass star-forming cores.

(v) RTDs from detected CH_3OH transitions yield rotational temperature and beam averaged column densities that are consistent with hot cores.

(vi) The $J = 3 - 2$ transition of C^{17}O towards MM6 shows a clear inverse P-Cygni profile that is a signature of protostellar infall.

(vii) From the $J = 1 - 0$ transition of the C^{18}O , we detect the presence of a large-scale molecular outflow in the direction of one of the lobes of the bipolar H_2 outflow. At higher resolution an additional collimated, bipolar outflow in the south-east and north-west direction is detected likely powered by MM2. This suggests that G19.88-0.53 harbours multiple outflows.

ACKNOWLEDGEMENTS

We thank the referee for valuable suggestions that have helped in improving the manuscript. The authors would like to thank Prof. Luis A. Zapata for kindly providing the fits images of the VLA maps of G19.88-0.53 presented in Zapata et al. (2006). CHIC acknowledges the support of the Department of Atomic Energy, Government of India, under the project 12-R&D-TFR-5.02-0700. We thank the staff of the GMRT, who made these observations possible. GMRT is run by the National Centre for Radio Astrophysics of the Tata Institute of Fundamental Research. We also thank the staff of UKIRT for their assistance in the observations. UKIRT is owned by the University of Hawaii (UH) and operated by the UH Institute for Astronomy. When some of the data reported here were acquired, UKIRT was supported by NASA and operated under an agreement among the University of

Hawaii, the University of Arizona, and Lockheed Martin Advanced Technology Center; operations were enabled through the cooperation of the East Asian Observatory. This paper uses the following ALMA data: ADS/JAO.ALMA#2017.1.00377.S. ALMA is a partnership of European Southern Observatory (ESO; representing its member states), NSF (USA), and NINS (Japan), together with NRC (Canada), MOST and ASIAA (Taiwan), and KASI (Republic of Korea), in cooperation with the Republic of Chile. The Joint ALMA Observatory is operated by ESO, AUI/NRAO and NAOJ. This research has used NASA/IPAC Infrared Science Archive, which is operated by the Jet Propulsion Laboratory, Caltech under contract with NASA. This publication also used data products from *Herschel* (ESA space observatory) and the ATLASGAL data products. The ATLASGAL project is a collaboration between the Max-Planck-Gesellschaft, the ESO, and the Universidad de Chile.

DATA AVAILABILITY

The original data underlying this article will be shared on reasonable request to the corresponding author.

REFERENCES

- Anglada G., 1996, in Taylor A. R., Paredes J. M., eds, ASP Conf. Ser., Vol. 93, Radio Emission from the Stars and the Sun. Astron. Soc. Pac., San Francisco, p. 3
- Beltrán M. T., Cesaroni R., Neri R., Codella C., 2011, *A&A*, 525, A151
- Benjamin R. A. et al., 2003, *PASP*, 115, 953
- Beuther H., Schilke P., Menten K. M., Motte F., Sridharan T. K., Wyrowski F., 2002a, *ApJ*, 566, 945
- Beuther H., Schilke P., Sridharan T. K., Menten K. M., Walmsley C. M., Wyrowski F., 2002b, *A&A*, 383, 892
- Beuther H., Walsh A., Schilke P., Sridharan T. K., Menten K. M., Wyrowski F., 2002c, *A&A*, 390, 289
- Beuther H., Schilke P., Menten K. M., Motte F., Sridharan T. K., Wyrowski F., 2005, *ApJ*, 633, 535
- Blake G. A., Sutton E. C., Masson C. R., Phillips T. G., 1987, *ApJ*, 315, 621
- Brogan C. L., Hunter T. R., Cyganowski C. J., Friesen R. K., Chandler C. J., Indebetouw R., 2011, *ApJ*, 739, L16
- Caratti o Garatti A., Stecklum B., Linz H., Garcia Lopez R., Sanna A., 2015, *A&A*, 573, A82
- Cesaroni R., Felli M., Jenness T., Neri R., Olmi L., Robberto M., Testi L., Walmsley C. M., 1999, *A&A*, 345, 949
- Chambers E. T., Jackson J. M., Rathborne J. M., Simon R., 2009, *ApJS*, 181, 360

- Chen X., Ellingsen S. P., Shen Z.-Q., Titmarsh A., Gan C.-G., 2011, *ApJS*, 196, 9
- Cheng Y., Tan J. C., Liu M., Kong S., Lim W., Andersen M., Da Rio N., 2018, *ApJ*, 853, 160
- Codella C., Beltrán M. T., Cesaroni R., Moscadelli L., Neri R., Vasta M., Zhang Q., 2013, *A&A*, 550, A81
- Csengeri T. et al., 2016, *A&A*, 585, A104
- Cyganowski C. J., Brogan C. L., Hunter T. R., 2007, *AJ*, 134, 346
- Cyganowski C. J. et al., 2008, *AJ*, 136, 2391
- Cyganowski C. J., Brogan C. L., Hunter T. R., Churchwell E., Zhang Q., 2011, *ApJ*, 729, 124
- Cyganowski C. J., Brogan C. L., Hunter T. R., Zhang Q., Friesen R. K., Indebetouw R., Chandler C. J., 2012, *ApJ*, 760, L20
- Davis C. J., Smith M. D., Stern L., Kerr T. H., Chiar J. E., 2003, *MNRAS*, 344, 262
- Davis C. J., Gell R., Khanzadyan T., Smith M. D., Jenness T., 2010, *A&A*, 511, A24
- De Buizer J. M., Vacca W. D., 2010, *AJ*, 140, 196
- Fazio G. G. et al., 2004, *ApJS*, 154, 10
- Froebrich D. et al., 2011, *MNRAS*, 413, 480
- Garay G., Brooks K. J., Mardones D., Norris R. P., 2003, *ApJ*, 587, 739
- Ge J. X., He J. H., Chen X., Takahashi S., 2014, *MNRAS*, 445, 1170
- Griffin M. J. et al., 2010, *A&A*, 518, L3
- Guzmán A. E., Garay G., Brooks K. J., 2010, *ApJ*, 725, 734
- Hatchell J., Fuller G. A., Millar T. J., 2001, *A&A*, 372, 281
- Hofner P., Cesaroni R., Kurtz S., Rosero V., Anderson C., Furuya R. S., Araya E. D., Molinari S., 2017, *ApJ*, 843, 99
- Ioannidis G., Froebrich D., 2012, *MNRAS*, 421, 3257
- Issac N., Tej A., Liu T., Varricatt W., Vig S., Ishwara Chandra C. H., Schultheis M., 2019, *MNRAS*, 485, 1775
- Kauffmann J., Pillai T., Shetty R., Myers P. C., Goodman A. A., 2010, *ApJ*, 716, 433
- Keto E. R., Ho P. T. P., Reid M. J., 1987, *ApJ*, 323, L117
- Klaassen P. D., Wilson C. D., Keto E. R., Zhang Q., Galván-Madrid R., Liu H. Y. B., 2011, *A&A*, 530, A53
- Krumholz M. R., Klein R. I., McKee C. F., 2007, *ApJ*, 656, 959
- Kuiper R., Klahr H., Beuther H., Henning T., 2010, *ApJ*, 722, 1556
- Kutner M. L., Tucker K. D., 1975, *ApJ*, 199, 79
- Lee H.-T., Takami M., Duan H.-Y., Karr J., Su Y.-N., Liu S.-Y., Froebrich D., Yeh C. C., 2012, *ApJS*, 200, 2
- Laurini S., Schilke P., Wyrowski F., Menten K. M., 2007, *A&A*, 466, 215
- Laurini S., Codella C., Gusdorf A., Zapata L., Gómez-Ruiz A., Testi L., Pillai T., 2013, *A&A*, 554, A35
- Liu S.-Y., Girart J. M., Remijan A., Snyder L. E., 2002, *ApJ*, 576, 255
- Liu T., Wu Y., Wu J., Qin S.-L., Zhang H., 2013, *MNRAS*, 436, 1335
- Liu T., Wu Y., Zhang H., 2013, *ApJ*, 776, 29
- López-Sepulcre A., Cesaroni R., Walmsley C. M., 2010, *A&A*, 517, A66
- López-Sepulcre A. et al., 2011, *A&A*, 526, L2
- Lovas F. J., 2004, *J. Phys. Chem. Ref. Data*, 33, 177
- Lucas P. W. et al., 2008, *MNRAS*, 391, 136
- Lumsden S. L., Hoare M. G., Urquhart J. S., Oudmaijer R. D., Davies B., Mottram J. C., Cooper H. D. B., Moore T. J. T., 2013, *ApJS*, 208, 11
- Marseille M., Bontemps S., Herpin F., van der Tak F. F. S., Purcell C. R., 2008, *A&A*, 488, 579
- Marston A. P. et al., 2004, *ApJS*, 154, 333
- Menten K. M., Walmsley C. M., Henkel C., Wilson T. L., 1986, *A&A*, 157, 318
- Miettinen O., Harju J., Haikala L. K., Pomréen C., 2006, *A&A*, 460, 721
- Molinari S. et al., 2010, *PASP*, 122, 314
- Motte F., Bontemps S., Louvet F., 2018, *ARA&A*, 56, 41
- Müller H. S. P., Schlöder F., Stutzki J., Winnewisser G., 2005, *J. Mol. Struct.*, 742, 215
- Noriega-Crespo A. et al., 2004, *ApJS*, 154, 352
- Obonyo W. O., Lumsden S. L., Hoare M. G., Purser S. J. D., Kurtz S. E., Johnston K. G., 2019, *MNRAS*, 486, 3664
- Onaka T., Mori T., Sakon I., Ardaseva A., 2016, *ApJ*, 829, 106
- Pickett H. M., Poynter R. L., Cohen E. A., Delitsky M. L., Pearson J. C., Müller H. S. P., 1998, *J. Quant. Spec. Radiat. Transf.*, 60, 883
- Pilbratt G. L. et al., 2010, *A&A*, 518, L1
- Poglitsch A. et al., 2010, *A&A*, 518, L2
- Purser S. J. D. et al., 2016, *MNRAS*, 460, 1039
- Qin S.-L., Zhao J.-H., Moran J. M., Marrone D. P., Patel N. A., Wang J.-J., Liu S.-Y., Kuan Y.-J., 2008, *ApJ*, 677, 353
- Qiu K., Zhang Q., Beuther H., Yang J., 2007, *ApJ*, 654, 361
- Qiu K., Zhang Q., Wu J., Chen H.-R., 2009, *ApJ*, 696, 66
- Ramsay Howat S. K. et al., 2004, in Moorwood A. F. M., Iye M., eds, *Proc. SPIE Conf. Ser. Vol. 5492, Ground-based Instrumentation for Astronomy*, SPIE, Bellingham, p. 1160
- Rathborne J. M., Jackson J. M., Chambers E. T., Simon R., Shipman R., Frieswijk W., 2005, *ApJ*, 630, L181
- Remijan A., Shiao Y.-S., Friedel D. N., Meier D. S., Snyder L. E., 2004, *ApJ*, 617, 384
- Ren Z., Wu Y., Zhu M., Liu T., Peng R., Qin S., Li L., 2012, *MNRAS*, 422, 1098
- Rodríguez L. F., 1997, in Reipurth B., Bertout C., eds, *Proc. IAU Symp. 182, Herbig-Haro Flows and the Birth of Stars*, Kluwer, Dordrecht, p. 83
- Rodríguez-Garza C. B., Kurtz S. E., Gómez-Ruiz A. I., Hofner P., Araya E. D., Kalenskii S. V., 2017, *ApJS*, 233, 4
- Roman-Duval J., Jackson J. M., Heyer M., Johnson A., Rathborne J., Shah R., Simon R., 2009, *ApJ*, 699, 1153
- Rosero V. et al., 2016, *ApJS*, 227, 25
- Rosero V. et al., 2019, *ApJ*, 880, 99
- Rygl K. L. J., Wyrowski F., Schuller F., Menten K. M., 2013, *A&A*, 549, A5
- Sanna A., Cesaroni R., Moscadelli L., Zhang Q., Menten K. M., Molinari S., Caratti o Garatti A., De Buizer J. M., 2014, *A&A*, 565, A34
- Schuller F. et al., 2009, *A&A*, 504, 415
- Shepherd D. S., Watson A. M., Sargent A. I., Churchwell E., 1998, *ApJ*, 507, 861
- Shepherd D. S., Testi L., Stark D. P., 2003, *ApJ*, 584, 882
- Smith M. D., Rosen A., 2005, *MNRAS*, 357, 1370
- Sridharan T. K., Beuther H., Schilke P., Menten K. M., Wyrowski F., 2002, *ApJ*, 566, 931
- Tan J. C., Beltrán M. T., Caselli P., Fontani F., Fuente A., Krumholz M. R., McKee C. F., Stolte A., 2014, *Protostars and Planets VI*, Univ. Arizona Press, Tucson, AZ, p. 149
- Towner A. P. M., Brogan C. L., Hunter T. R., Cyganowski C. J., Friesen R. K., 2019, *ApJ*, 875, 135
- Urquhart J. S. et al., 2009, *A&A*, 501, 539
- Varricatt W. P., Davis C. J., Ramsay S., Todd S. P., 2010, *MNRAS*, 404, 661
- Watson C. et al., 2008, *ApJ*, 681, 1341
- Widmann F., Beuther H., Schilke P., Stanke T., 2016, *A&A*, 589, A29
- Williams J. P., de Geus E. J., Blitz L., 1994, *ApJ*, 428, 693
- Wirström E. S. et al., 2011, *A&A*, 533, A24
- Wu Y., Qin S.-L., Guan X., Xue R., Ren Z., Liu T., Huang M., Chen S., 2009, *ApJ*, 697, L116
- Zapata L. A., Rodríguez L. F., Ho P. T. P., Beuther H., Zhang Q., 2006, *AJ*, 131, 939
- Zapata L. A., Palau A., Ho P. T. P., Schilke P., Garrod R. T., Rodríguez L. F., Menten K., 2008, *A&A*, 479, L25
- Zhang Q., Hunter T. R., Brand J., Sridharan T. K., Molinari S., Kramer M. A., Cesaroni R., 2001, *ApJ*, 552, L167

APPENDIX A:

Table A1. Spectroscopic parameters of the $A - \text{CH}_3\text{OH}$ and $E - \text{CH}_3\text{OH}$ lines detected towards G19.88-0.53 taken from the spectroscopic data bases, CDMS and JPL from *spalatalogue*.

Transition J_k	Frequency (MHz)	E_u (K)	$S\mu^2$ (debye ²)
$A - \text{CH}_3\text{OH}$			
$7_0 - 6_0$	338408.698	64.98	5.66
$7_6 - 6_6$	338442.367	258.7	3.01
$7_5 - 6_5$	338486.322	202.88	5.57
$7_4 - 6_4$	338512.632	145.33	3.82
$7_3 - 6_3$	338543.152	114.79	4.61
$7_2 - 6_2$	338639.802	102.72	5.23
$2_2 - 3_1$	340141.143	44.67	0.31
$E - \text{CH}_3\text{OH}$			
$3_3 - 4_2$	337135.853	61.64	0.99
$7_0 - 6_0$	338124.488	78.08	5.65
$7_{-1} - 6_{-1}$	338344.588	70.55	5.55
$7_6 - 6_6$	338430.981	253.95	1.50
$7_{-5} - 6_{-5}$	338456.521	189.00	2.76
$7_5 - 6_5$	338475.217	201.06	2.76
$7_{-4} - 6_{-4}$	338504.065	152.89	3.81
$7_4 - 6_4$	338530.256	160.99	3.82
$7_{-3} - 6_{-3}$	338559.963	127.71	4.64
$7_3 - 6_3$	338583.216	112.71	4.63
$7_1 - 6_1$	338614.936	86.05	5.68
$7_2 - 6_2$	338721.693	87.26	5.14

Table A2. $A - \text{CH}_3\text{OH}$ and $E - \text{CH}_3\text{OH}$ lines towards MM1, MM3, and MM4 of G19.88-0.53. Columns 1 and 2 are the transitions and the corresponding frequencies, respectively. Columns 3–5 are the parameters and the uncertainties from the Gaussian fits to each line; they are line flux ($\int I_\nu dV$), LSR velocity (V_{LSR}), and the line width (ΔV). Column 6 is the optical depth for each transition with two values, the first for T_{rot} and the second for $T_d = 18.6$ K, respectively.

Transition J_k	Frequency (MHz)	V_{LSR} (km s ⁻¹)	$\int I_\nu dV$ (Jy beam ⁻¹ km s ⁻¹)	ΔV (km s ⁻¹)	$\tau_{T_{\text{rot}}}/\tau_{T_d}$
$A - \text{CH}_3\text{OH}$					
$7_0 - 6_0$	338408.698	43.6 \pm 0.4	40.3 \pm 0.9	4.1 \pm 0.4	0.112/0.496
$7_6 - 6_6$	338442.367	44.9 \pm 0.1	1.6 \pm 0.1	5.6 \pm 0.3	0.003/0.015
$7_5 - 6_5$	338486.322	44.7 \pm 0.1	2.5 \pm 0.1	5.4 \pm 0.2	0.005/0.023
$7_4 - 6_4$	338512.632	43.7 \pm 0.1	11.9 \pm 0.5	4.2 \pm 0.2	0.032/0.142
$7_3 - 6_3$	338543.152	44.8 \pm 0.4	15.7 \pm 0.4	5.4 \pm 0.4	0.033/0.147
$7_2 - 6_2$	338639.802	43.9 \pm 0.4	9.0 \pm 0.6	4.3 \pm 0.4	0.024/0.106
$2_2 - 3_1$	340141.143	44.3 \pm 0.03	2.4 \pm 0.1	4.7 \pm 0.1	0.006/0.025
$E - \text{CH}_3\text{OH}$					
$3_3 - 4_2$	337135.853	44.6 \pm 0.1	1.8 \pm 0.05	5.0 \pm 0.1	0.004/0.016
$7_0 - 6_0$	338124.488	43.6 \pm 0.01	23.9 \pm 0.2	3.7 \pm 0.03	0.073/0.324
$7_{-1} - 6_{-1}$	338344.588	43.6 \pm 0.01	36.4 \pm 0.2	3.9 \pm 0.02	0.105/0.466
$7_6 - 6_6$	338430.981	44.9 \pm 0.1	1.5 \pm 0.1	6.0 \pm 0.3	0.003/0.013
$7_{-5} - 6_{-5}$	338456.521	44.8 \pm 0.2	1.9 \pm 0.2	5.0 \pm 0.6	0.004/0.019
$7_5 - 6_5$	338475.217	44.8 \pm 1.1	1.7 \pm 0.8	4.7 \pm 2.1	0.004/0.018
$7_{-4} - 6_{-4}$	338504.065	44.0 \pm 0.1	4.0 \pm 0.2	6.1 \pm 0.4	0.007/0.033
$7_4 - 6_4$	338530.256	44.3 \pm 0.2	3.2 \pm 0.3	6.2 \pm 0.7	0.006/0.026
$7_{-3} - 6_{-3}$	338559.963	44.1 \pm 0.1	4.7 \pm 0.3	4.9 \pm 0.3	0.011/0.048
$7_3 - 6_3$	338583.216	43.9 \pm 0.1	6.9 \pm 0.3	4.7 \pm 0.2	0.017/0.075
$7_1 - 6_1$	338614.936	43.7 \pm 0.4	18.9 \pm 0.5	3.9 \pm 0.4	0.055/0.246
$7_2 - 6_2$	338721.693	44.4 \pm 0.4	30.3 \pm 0.7	4.0 \pm 0.4	0.085/0.380

Table A3. Same as Table A2 for MM2 towards G19.88-0.53.

Transition (MHz)	Frequency (km s ⁻¹)	V_{LSR} (Jy beam ⁻¹ km s ⁻¹)	$\int I_{\nu} dV$ (km s ⁻¹)	ΔV	$\tau_{\text{rot}}/\tau_{T_d}$
<i>A</i> – CH ₃ OH					
7 ₀ – 6 ₀	338408.698	44.1 ± 0.02	27.5 ± 0.2	4.1 ± 0.04	0.054/0.335
7 ₆ – 6 ₆	338442.367	45.6 ± 0.4	2.8 ± 0.5	5.0 ± 1.1	0.004/0.028
7 ₅ – 6 ₅	338486.322	45.4 ± 0.2	3.8 ± 0.3	5.2 ± 0.4	0.006/0.037
7 ₄ – 6 ₄	338512.632	44.4 ± 0.1	11.3 ± 0.6	4.3 ± 0.3	0.021/0.131
7 ₃ – 6 ₃	338543.152	45.5 ± 0.2	14.3 ± 0.9	5.4 ± 0.4	0.022/0.135
7 ₂ – 6 ₂	338639.802	44.5 ± 0.02	8.2 ± 0.1	4.0 ± 0.1	0.016/0.102
2 ₂ – 3 ₁	340141.143	45.3 ± 0.4	3.6 ± 0.1	5.0 ± 0.4	0.006/0.036
<i>E</i> – CH ₃ OH					
3 ₃ – 4 ₂	337135.853	45.5 ± 0.1	2.3 ± 0.1	4.4 ± 0.1	0.004/0.026
7 ₀ – 6 ₀	338124.488	44.3 ± 0.4	18.7 ± 0.4	4.2 ± 0.4	0.036/0.227
7 ₋₁ – 6 ₋₁	338344.588	44.2 ± 0.01	25.7 ± 0.1	4.1 ± 0.02	0.051/0.316
7 ₆ – 6 ₆	338430.981	45.7 ± 0.4	2.3 ± 0.4	4.7 ± 0.9	0.004/0.025
7 ₋₅ – 6 ₋₅	338456.521	45.3 ± 0.4	3.2 ± 0.1	5.0 ± 0.4	0.005/0.032
7 ₅ – 6 ₅	338475.217	45.3 ± 0.2	3.0 ± 0.2	4.7 ± 0.4	0.005/0.032
7 ₋₄ – 6 ₋₄	338504.065	45.0 ± 0.2	4.7 ± 0.4	5.3 ± 0.5	0.007/0.045
7 ₄ – 6 ₄	338530.256	45.2 ± 0.1	4.1 ± 0.1	5.2 ± 0.2	0.006/0.040
7 ₋₃ – 6 ₋₃	338559.963	44.9 ± 0.2	5.3 ± 0.5	4.5 ± 0.5	0.009/0.059
7 ₃ – 6 ₃	338583.216	44.8 ± 0.1	6.9 ± 0.2	4.6 ± 0.2	0.012/0.076
7 ₁ – 6 ₁	338614.936	44.4 ± 0.4	15.4 ± 0.4	4.0 ± 0.4	0.031/0.193
7 ₂ – 6 ₂	338721.693	44.9 ± 0.01	23.9 ± 0.1	4.3 ± 0.01	0.045/0.280

Table A4. Same as Table A2 for MM5 and MM6 towards G19.88-0.53.

Transition (MHz)	Frequency (km s ⁻¹)	V_{LSR} (Jy beam ⁻¹ km s ⁻¹)	$\int I_{\nu} dV$ (km s ⁻¹)	ΔV	$\tau_{\text{rot}}/\tau_{T_d}$
<i>A</i> – CH ₃ OH					
7 ₀ – 6 ₀	338408.698	42.7 ± 0.01	9.6 ± 0.6	2.1 ± 0.04	0.091/0.230
7 ₄ – 6 ₄	338512.632	42.8 ± 0.04	2.3 ± 0.1	3.1 ± 0.1	0.015/0.038
7 ₃ – 6 ₃	338543.152	44.0 ± 0.05	3.2 ± 0.1	4.2 ± 0.1	0.015/0.039
7 ₂ – 6 ₂	338639.802	42.9 ± 0.02	1.6 ± 0.03	2.9 ± 0.1	0.011/0.027
2 ₂ – 3 ₁	340141.143	43.0 ± 0.1	0.2 ± 0.02	2.5 ± 0.3	0.002/0.005
<i>E</i> – CH ₃ OH					
7 ₀ – 6 ₀	338124.488	42.8 ± 0.01	4.5 ± 0.2	2.1 ± 0.04	0.043/0.109
7 ₋₁ – 6 ₋₁	338344.588	42.9 ± 0.01	13.3 ± 0.1	2.5 ± 0.02	0.107/0.271
7 ₋₃ – 6 ₋₃	338559.963	42.5 ± 0.1	0.3 ± 0.04	2.3 ± 0.4	0.003/0.007
7 ₃ – 6 ₃	338583.216	42.7 ± 0.4	0.8 ± 0.3	2.7 ± 1.0	0.006/0.015
7 ₁ – 6 ₁	338614.936	43.1 ± 0.1	5.5 ± 0.2	3.0 ± 0.1	0.036/0.092
7 ₂ – 6 ₂	338721.693	43.7 ± 0.02	9.4 ± 0.1	3.0 ± 0.03	0.062/0.158

This paper has been typeset from a \LaTeX file prepared by the author.